A Novel Transformation of the Ice Sheet Stokes Equations and Some of its Properties and Applications

John K. Dukowicz

Guest Scientist, Group T-3, Los Alamos National Laboratory,

Los Alamos, New Mexico, 87545, USA

Correspondence to: John K. Dukowicz (jn.dk@outlook.com)

Abstract.   We introduce a novel transformation of the Stokes equations into a form that closely resembles the shallow Blatter-Pattyn equations. The two forms differ by only a few additional terms, while their variational formulations differ by only a single term in each horizontal direction. Specifically, the variational formulation of the Blatter-Pattyn model drops the vertical velocity in the second invariant of the strain rate tensor. Here we make use of the new transformation in two different ways. First, we consider incorporating the transformed equations into a code that can be very easily converted from a Stokes to a Blatter-Pattyn model, and vice-versa, by switching these terms on or off. This may be generalized so that the Stokes model is switched on adaptively only where the Blatter-Pattyn model loses accuracy. Second, the key role played by the vertical velocity in the Blatter-Pattyn approximation motivates new approximations that improve on the Blatter-Pattyn model. These applications require a grid that enables the discrete continuity equation to be invertible for the vertical velocity in terms of the horizontal velocity components. Examples of such grids, such as the first order P1-E0 grid and the second order P2-E1 grid, are given in both 2D and 3D. It should be noted, however, that the transformed Stokes model has the same type of gravity forcing as the Blatter-Pattyn model, determined by the ice surface slope, thereby forgoing some of the grid-generality of the traditional formulation of the Stokes model.

1 Introduction

Concern and uncertainty about the magnitude of sea level rise due to melting of the Greenland and Antarctic ice sheets have led to increased interest in improved ice sheet and glacier modeling. The gold standard is a Stokes model (i.e., a model that solves the nonlinear, non-Newtonian Stokes system of equations for incompressible ice sheet dynamics) because it is applicable to all geometries and flow regimes. However, the Stokes model is computationally demanding and expensive to solve. It is a nonlinear, three-dimensional model involving four variables, namely, the three velocity components and pressure. In addition, pressure is a Lagrange multiplier enforcing incompressibility

October 15, 2024

38 and this creates a more difficult indefinite "saddle point" problem. As a result, full-

39 Stokes models exist but are not commonly used in practice (examples are FELIX-S, Leng

40 et al., 2012; Elmer/Ice, Gagliardini et al., 2013).

42   Because of these difficulties there is much interest in simpler and cheaper

43 approximate models. There is a hierarchy of very simple models such as the shallow ice

44 (SIA) and shallow-shelf (SSA) models, and there are also various more accurate higher-

45 order approximations. These culminate in the Blatter-Pattyn (BP) approximation

46 (Blatter, 1995; Pattyn, 2003), which is currently used in production code packages such

47 as ISSM (Larour et al., 2012), MALI (Hoffman et al., 2018; Tezaur et al., 2015) and

48 CISM (Lipscomb et al., 2019). This approximation is based on the assumption of a small

49 ice sheet aspect ratio, i.e., $\varepsilon = H/L \ll 1$, where H, L are the vertical and horizontal

50 length scales, and consequently it eliminates certain stress terms and implicitly assumes

51 small basal slopes. Both the Stokes and Blatter-Pattyn models are described in detail in

52 Dukowicz et al. (2010), hereafter referred to as DPL (2010). Although the Blatter-Pattyn

53 model is reasonably accurate for large-scale motions, accuracy deteriorates for small

54 horizontal scales, less than about five ice thicknesses in the ISMIP–HOM model

55 intercomparison (Pattyn et al., 2008; Perego et al., 2012), or below a 1 km resolution as

56 found in a detailed comparison with full Stokes calculations (Rückamp et al, 2022). This

57 can become particularly important for calculations involving details near the grounding

58 line where the full accuracy of the Stokes model is needed (Nowicki and Wingham,

59 2008). Attempts to address the problem while avoiding the use of full Stokes solvers

60 include variable grid resolution coupled with a Blatter-Pattyn solver (Hoffman et al.,

61 2018) and variable model complexity, where a Stokes solver is embedded locally in a

62 lower order model (Seroussi et al., 2012). Better approximations, more accurate than

63 Blatter-Pattyn but cheaper than Stokes, are currently not available.

64

65   The present paper introduces two innovations that may begin to address some of

66 these issues. The first is a novel transformation of the Stokes model, described in §3,

67 which puts it into a form closely resembling the Blatter-Pattyn model and differing only

68 by the presence of a few extra terms. This allows a code to be switched over from Stokes

69 to Blatter-Pattyn, and vice-versa, globally or locally, by the use of a single parameter that

70 turns off these extra terms. As a result, variable model complexity can be very simply

71 implemented, as described in §6.1. The second innovation is the introduction of new

October 15, 2024

72 finite element discretizations that decouple the discrete continuity equation and allow it to
73 be solved for the vertical velocity in terms of the horizontal velocity components.
74 Several elements used to construct such grids are described in Appendix C in both 2D
75 and 3D, primarily the first order P1-E0 and second order P2-E1 elements (these two
76 elements are novel and are so-named because pressures are located on vertical grid
77 edges). Within the framework of the transformed Stokes model these grids facilitate new
78 approximations that improve on the Blatter-Pattyn approximation so that it is no longer
79 strictly limited to a small ice sheet aspect ratio. We describe two such approximations in
80 §6.2. There is another very significant benefit. An ice sheet Stokes model is
81 conventionally discretized as a constrained minimization problem requiring special
82 "stable" finite elements for solution. However, on these new grids the corresponding
83 model can be formulated as an inherently stable unconstrained minimization problem, as
84 demonstrated in §4.3.2.
85
86 **2 The Standard Formulation of the Stokes Ice Sheet Model**
87 **2.1 The Assumed Ice Sheet Configuration**
88
89 An ice sheet may be divided into two parts, a part in contact with the bed and a floating
90 ice shelf located beyond the grounding line. The Stokes ice sheet model is capable of
91 describing the flow of an arbitrarily shaped ice sheet, including a floating ice shelf as
92 illustrated in Fig. 1, given appropriate boundary conditions (e.g., Cheng et al., 2020).
93 One limitation of the methods proposed here, in common with the Blatter-Pattyn model,
94 will be that there should be just one upper and one basal surface, as is the case in Fig. 1.
95 Here we will only consider a fully grounded ice sheet with periodic lateral boundary
96 conditions, i.e., no ice shelf, although ice shelves can also be handled in general.
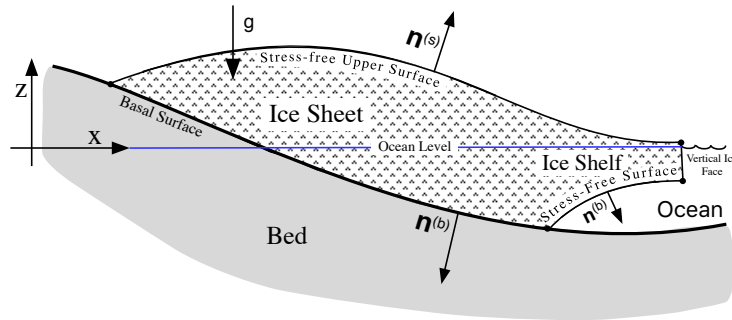
97
98
99 **Figure 1** A simplified illustration of the admissible ice sheet configuration.
100

October 15, 2024

101

102   Referring to Fig. 1, the entire surface of the ice sheet is denoted by S. An upper

103   surface, labeled S_S and specified by $\varsigma_s(x,y,z) = z - z_s(x,y) = 0$, is exposed to the

104   atmosphere and thus experiences stress-free boundary conditions. The bottom or basal

105   surface, denoted by S_B and specified by $\varsigma_b(x,y,z) = z - z_b(x,y) = 0$, is in contact with

106   the bed. The basal surface may be subdivided into two sections, $S_B = S_{B1} \cup S_{B2}$, where

107   S_{B1}, specified by $z = z_{b1}(x,y)$, is the part where ice is frozen to the bed (a no-slip

108   boundary condition), and S_{B2}, specified by $z = z_{b2}(x,y)$, is where frictional sliding

109   occurs. We assume Cartesian coordinates such that $x_i = (x,y,z)$ are position coordinates

110   with $z = 0$ at the ocean surface, and the index $i \in \{x,y,z\}$ represents the three Cartesian

111   indices. Later we shall have occasion to introduce the restricted index $(i) \in \{x,y\}$ to

112   represent just the two horizontal indices. Note that this is equivalent to applying a

113   projection operator, i.e., $u_{(i)} = P_i(u) = (u,v,0)$, but it is more compact. Unit normal

114   vectors appropriate for the ice sheet configuration of Fig. 1 are given by

115
$$n_i = (n_x, n_y, n_z) = \frac{\partial \varsigma_s(x,y,z)/\partial x_i}{|\partial \varsigma_s(x,y,z)/\partial x_i|} = \frac{(-\partial z_s/\partial x, -\partial z_s/\partial y, 1)}{\sqrt{1 + (\partial z_s/\partial x)^2 + (\partial z_s/\partial y)^2}} \quad \text{at surface } S_S,$$
$$n_i = (n_x, n_y, n_z) = -\frac{\partial \varsigma_b(x,y,z)/\partial x_i}{|\partial \varsigma_b(x,y,z)/\partial x_i|} = \frac{(\partial z_b/\partial x, \partial z_b/\partial y, -1)}{\sqrt{1 + (\partial z_b/\partial x)^2 + (\partial z_b/\partial y)^2}} \quad \text{at surface } S_B.$$
(1)

116

117   **2.2 The Stokes Equations**

118

119   The Stokes model is a system of nonlinear partial differential equations and associated

120   boundary conditions (Greve and Blatter, 2009; DPL, 2010). In a Cartesian coordinate

121   system the Stokes equations, the three momentum equations and the continuity equation,

122   for the three velocity components $u_i = (u,v,w)$ and the pressure P are given by

123
$$\frac{\partial \tau_{ij}}{\partial x_j} - \frac{\partial P}{\partial x_i} + \rho g_i = 0 ,$$
(2)

October 15, 2024

124
$$\frac{\partial u_i}{\partial x_i} = 0 , \tag{3}$$

125 where ρ is the density, and g_i is the acceleration vector due to gravity, arbitrarily

126 oriented in general but here taken to be in the negative z-direction, $g_i = (0,0,-g)$.

127 Repeated indices imply summation (the Einstein notation). The deviatoric stress tensor

128 τ_{ij} is given by

129
$$\tau_{ij} = 2\mu_n \dot{\varepsilon}_{ij} , \tag{4}$$

130 where the strain rate tensor is

131
$$\dot{\varepsilon}_{ij} = \frac{1}{2}\left(\frac{\partial u_i}{\partial x_j} + \frac{\partial u_j}{\partial x_i} \right) , \tag{5}$$

132 the nonlinear ice viscosity μ_n is a defined by

133
$$\mu_n = \eta_0 \left(\dot{\varepsilon}^2 \right)^{(1-n)/2n} , \tag{6}$$

134 and $\dot{\varepsilon}^2 = \dot{\varepsilon}_{ij}\dot{\varepsilon}_{ij}/2$ is the second invariant of the strain rate tensor that may be written out

135 in full as follows

136
$$\dot{\varepsilon}^2 = \frac{1}{2}\left[\left(\frac{\partial u}{\partial x}\right)^2 + \left(\frac{\partial v}{\partial y}\right)^2 + \left(\frac{\partial w}{\partial z}\right)^2 \right] + \frac{1}{4}\left[\left(\frac{\partial u}{\partial y} + \frac{\partial v}{\partial x}\right)^2 + \left(\frac{\partial u}{\partial z} + \frac{\partial w}{\partial x}\right)^2 + \left(\frac{\partial v}{\partial z} + \frac{\partial w}{\partial y}\right)^2 \right] . \tag{7}$$

137 Note that the second invariant is a positive quantity, i.e., $\dot{\varepsilon}^2 \geq 0$. As usual, ice is assumed

138 to obey Glen's flow law, where n is the Glen's law exponent ($n = 1$ for a linear

139 Newtonian fluid. Typically $n = 3$ in ice sheet modeling, resulting in a nonlinear non-

140 Newtonian fluid). The coefficient η_0 is defined by $\eta_0 = A^{-1/n}/2$, where A is an ice flow

141 factor, here taken to be a constant but in general depending on temperature and other

142 variables (see Schoof and Hewitt, 2013). The three-dimensional Stokes system requires a

143 set of boundary conditions at every bounding surface, each set being composed of three

144 components. Aside from the periodic lateral boundary conditions used in our test

145 problems, the relevant boundary conditions are given as follows

146   (1) Stress-free boundary conditions on surfaces S_S not in contact with the bed, such

147 as the upper surface S_S:

148
$$\tau_{ij}n_j - Pn_t = 0 . \tag{8}$$

October 15, 2024

149   (2) No-slip or frozen to the bed conditions on surface segment S_{B1}:

$$u_i = 0 \tag{9}$$

151   (3) Frictional tangential sliding conditions on surface segment S_{B2} in two parts:

152   (3a) A single condition enforcing tangential flow at the basal surface:

$$u_i n_i = 0 . \tag{10}$$

154   (3b) Two conditions specifying the horizontal components of the tangential

155   frictional stress force vector, as follows

$$\tau_{(i)j} n_j - \tau_n n_{(i)} + \tau_{(i)}^S = 0 , \tag{11}$$

157   where $\tau_n = n_i \tau_{ij} n_j$ is the normal component of the shear stress, and τ_i^S is a specified

158   interfacial shear stress, tangential to the bed $\left(n_i \tau_i^S = 0 \right)$. The tangential shear stress or

159   traction is obtained as in DPL (2010) by subtracting out the normal component from the

160   shear stress. However, the three components of the tangential shear stress are not

161   independent because they already satisfy the tangency condition at the basal surface and

162   therefore we retain only the horizontal components. The interfacial shear stress τ_i^S is

163   potentially a complicated function of position and velocity (e.g., Schoof, 2010).

164   However, here we assume only simple linear frictional sliding,

$$\tau_i^S = \beta(x) u_i , \tag{12}$$

166   where $\beta(x) > 0$ is a position-dependent drag law coefficient. For simplicity we assume

167   there is no melting or refreezing at the bed resulting in vertical inflows or outflows. If

168   needed, these can be easily added to (10) (Dukowicz et al., 2010; Heinlein et al., 2022).

169

170   **2.3 The Stokes Variational Principle**

171

172   A variational principle, if available, is usually the most compact way of representing a

173   particular problem. The Stokes model possesses a variational principle that is

174   particularly useful for discretization purposes and for the specification of boundary

175   conditions (see DPL, 2010, and Chen et al., 2013, for a fuller description of the

176   variational principle applied to ice sheet modeling). There are a number of significant

177   advantages. For example, all boundary conditions are conveniently incorporated in the

178   variational formulation, all terms in the variational functional, including boundary

179   condition terms, contain lower order derivatives than in the momentum equations, and the

October 15, 2024

180   resulting discretization automatically involves a symmetric matrix. In discretizing the

181   momentum equations, stress terms at boundaries involve derivatives that would normally

182   have to be evaluated using less accurate one-sided approximations. This problem does

183   not arise in the variational formulation since all terms are evaluated in the interior.

184   Finally, stress-free boundary conditions, as at the upper surface for example, need not be

185   specified at all since they are automatically incorporated in the functional as natural

186   boundary conditions. In discrete applications, the variational method presented here is

187   closely related to the Galerkin finite element method, a subset of the weak formulation

188   method in which the test and trial functions are the same (see Schoof, 2010, and earlier

189   references contained therein in connection with the Blatter-Pattyn model).

190

191   The variational functional for the standard Stokes model may be written in two

192   alternative forms:

193   (1) Basal boundary conditions imposed using Lagrange multipliers:

194
$$\mathcal{A}[u_i, P, \lambda_i, \Lambda] = \int_V dV \left[\frac{4n}{n+1} \eta_0 \left(\dot{\varepsilon}^2 \right)^{(1+n)/2n} - P \frac{\partial u_i}{\partial x_i} + \rho g w \right]$$
$$+ \int_{S_{B1}} dS \, \lambda_i u_i + \int_{S_{B2}} dS \left[\Lambda u_i n_i + \frac{1}{2} \beta(x) \, u_i u_i \right],$$
(13)

195   where λ_i and Λ are Lagrange multipliers used to enforce the no-slip condition and

196   frictional tangential sliding, respectively. As in DPL (2010), arguments enclosed in

197   square brackets, here $u_i, P, \lambda_i, \Lambda$, indicates those functions that are subject to variation as

198   arguments of the functional.

199   (2) Basal boundary conditions imposed by direct substitution:

200   In this case, the two conditions (9), (10) are used directly in the functional to specify all

201   three velocity components u_i in the first case, and the vertical velocity w in terms of the

202   horizontal velocity components in the second case, along the entire basal boundary in

203   both the volume and surface integrals in (13). However, this can only be done in the

204   discrete formulation of the functional since only then are boundary values of velocity

205   accessible (although they are always accessible in the surface integral terms). In

206   particular, the tangential flow condition (10) is used in the following form,

207
$$w = -\frac{u_{(i)} n_{(i)}}{n_z} = u_{(i)} \frac{\partial z_b}{\partial x_{(i)}},$$
(14)

208   to eliminate w on the basal boundary segment S_{B2} of the variational functional, to obtain

October 15, 2024

$$\mathcal{A}[u_i, P] = \int_V dV \left[\frac{4n}{n+1} \eta_0 \left(\dot{\varepsilon}^2 \right)^{(1+n)/2n} - P \frac{\partial u_i}{\partial x_i} + \rho g w \right]$$
$$+ \frac{1}{2} \int_{S_{B2}} dS \, \beta(x) \left(u_{(i)} u_{(i)} + \left(u_{(i)} n_{(i)} / n_z^{(b2)} \right)^2 \right).$$

(15)

210   We emphasize again that boundary conditions (9) and (14) must also be applied in the
211   volume integral part of the discretized functional (15) as part of direct substitution to
212   replace velocity variables that lie on the basal boundary.

213

214   As described in DPL (2010), a variational procedure yields the full set of Euler-
215   Lagrange equations and boundary conditions that specify the standard Stokes model,
216   equivalent to (2)-(11). In the case of (13), the system determines all the discrete variables
217   specified on the mesh: the velocity components and the pressure, u_i, P, as well as the
218   Lagrange multipliers, λ_i, Λ. In the direct substitution case, (15), the numerical solution
219   determines only the pressure P and velocity variables u_i other than those that were
220   directly prescribed as boundary conditions in (9) or (14). These known values of
221   boundary velocity are then added a posteriori. As a result, the problem is smaller and
222   simpler and so direct substitution is the method primarily used in the paper.

223

224   **3. A Transformation of the Stokes Model**
225   **3.1 Origin of the Transformation**

226

227   The transformation is motivated by the Blatter-Pattyn approximation. Consider the
228   vertical component of the momentum equation and the corresponding stress-free upper
229   surface boundary condition in the Blatter-Pattyn approximation (from DPL, 2010, for
230   example), which are given by

$$\frac{\partial}{\partial z} \left(2\mu_n \frac{\partial w}{\partial z} \right) - \frac{\partial P}{\partial z} - \rho g = 0,$$
$$\left(2\mu_n \frac{\partial w}{\partial z} - P \right) n_z = 0 \quad \text{at} \quad z = z_s(x, y).$$

(16)

232   These equations may be rewritten in the form

$$\frac{\partial}{\partial z}\left(P - 2\mu_n \frac{\partial w}{\partial z} + \rho g\left(z - z_s(x,y)\right)\right) = 0,$$

$$\left(P - 2\mu_n \frac{\partial w}{\partial z} + \rho g\left(z - z_s(x,y)\right)\right)n_z = 0 \quad \text{at} \quad z = z_s(x,y), \tag{17}$$

234   suggesting a new variable $\tilde{P}$, to be called the transformed pressure, as follows

$$\tilde{P} = P - 2\mu_n \frac{\partial w}{\partial z} + \rho g\left(z - z_s(x,y)\right), \tag{18}$$

236   which simplifies system (17) to give

$$\frac{\partial \tilde{P}}{\partial z} = 0,$$

$$\tilde{P} n_z = 0 \quad \text{at} \quad z = z_s(x,y). \tag{19}$$

238   This is a complete one-dimensional partial differential system, that, when integrated from
239   the top surface down yields

$$\tilde{P} = 0. \tag{20}$$

241   Thus, the transformed pressure vanishes in the Blatter-Pattyn case. The definition (18)
242   forms the basis of the present transformation but we also use the continuity equation to
243   eliminate $\partial w / \partial z$ as is done in the Blatter-Pattyn approximation (e.g., Pattyn, 2003).

244   Therefore, the transformation consists of eliminating P and $\partial w / \partial z$ in the Stokes system
245   (2), (4)-(11) (i.e., everywhere except in the continuity equation (3) itself) by means of

$$P = \tilde{P} - 2\mu_n\left(\frac{\partial u}{\partial x} + \frac{\partial v}{\partial y}\right) + \rho g\left(z_s - z\right), \tag{21}$$

$$\frac{\partial w}{\partial z} = -\left(\frac{\partial u}{\partial x} + \frac{\partial v}{\partial y}\right). \tag{22}$$

248
249   The pressure P in the standard Stokes system is primarily a Lagrange multiplier
250   enforcing incompressibility, but with a very large hydrostatic component. The
251   transformation eliminates the hydrostatic pressure from $\tilde{P}$, as illustrated in Fig. 2 where
252   the two pressures are compared. The transformed pressure $\tilde{P}$ is some three orders of
253   magnitude smaller than the standard Stokes pressure P primarily because of the absence
254   of hydrostatic pressure.

October 15, 2024
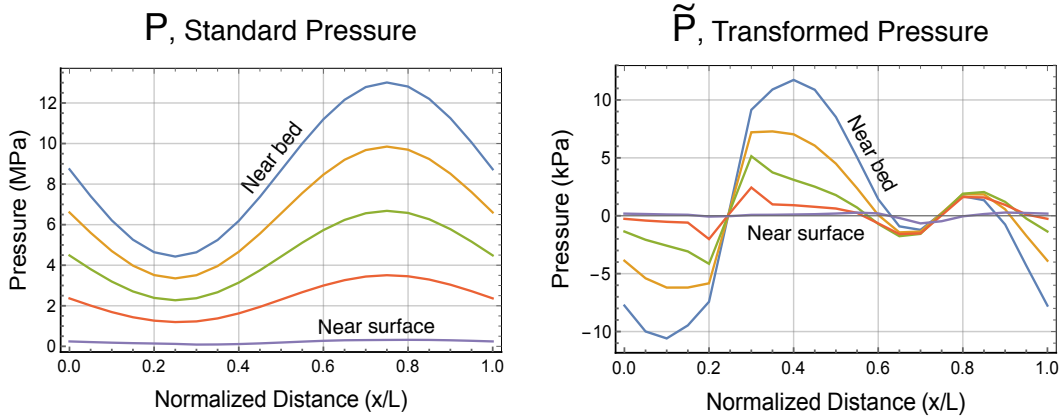
Figure 2. Standard pressure P compared to the transformed pressure $\tilde{P}$ in Exp. B from

the ISMIP–HOM model intercomparison (Pattyn et al., 2008) at L = 10 km.

Note that P is in MPa while $\tilde{P}$ is in kPa.

The transformed pressure $\tilde{P}$ is again a Lagrange multiplier enforcing

incompressibility. Alternatively, since $\tilde{P} = 0$ in the Blatter-Pattyn approximation, the

transformed pressure may be written as $\tilde{P} = P - P_{BP}$, where

$$P_{BP} = -2\mu_n\left(\frac{\partial u}{\partial x} + \frac{\partial v}{\partial y}\right) + \rho g\left(z_s - z\right)$$

is the effective Blatter-Pattyn pressure (Tezaur et al., 2015). As a result, $P = P_{BP} + \tilde{P}$ and

therefore $\tilde{P}$ is actually the "Stokes" correction to the Blatter-Pattyn pressure.

3.2 The Transformed Stokes Equations

Introducing (21), (22) into the Stokes system of equations (2)-(11) results in the

following transformed Stokes system:

$$\frac{\partial \tilde{\tau}_{ij}}{\partial x_j} - \hat{\xi}\frac{\partial \tilde{P}}{\partial x_i} - \rho g \frac{\partial z_s}{\partial x_{(i)}} = 0 \,, \tag{23}$$

$$\hat{\xi}\frac{\partial u_i}{\partial x_i} = 0 \,, \tag{24}$$

where quantities that are modified in the transformation are indicated by a tilde, e.g., $\tilde{P}$.

Here and in the following we will be using dummy variables $\xi, \hat{\xi}$ to indicate terms that

October 15, 2024

275 are absent in the Blatter-Blatter approximation. Corresponding to (4) the modified

276 Stokes deviatoric stress tensor $\tilde{\tau}_{ij}$ is given by

$$\tilde{\tau}_{ij} = 2\tilde{\mu}_n \left(\tilde{\dot{\varepsilon}}_{ij} + \frac{\partial u_{(i)}}{\partial x_{(i)}} \delta_{ij} \right), \tag{25}$$

278 where δ_{ij} is the Kronecker delta, the modified strain rate tensor $\tilde{\dot{\varepsilon}}_{ij}$, corresponding to (5),

279 is given by

$$\tilde{\dot{\varepsilon}}_{ij} = \begin{bmatrix} \dfrac{\partial u}{\partial x} & \dfrac{1}{2}\left(\dfrac{\partial u}{\partial y}+\dfrac{\partial v}{\partial x}\right) & \dfrac{1}{2}\left(\dfrac{\partial u}{\partial z}+\xi\dfrac{\partial w}{\partial x}\right) \\[2mm] \dfrac{1}{2}\left(\dfrac{\partial u}{\partial y}+\dfrac{\partial v}{\partial x}\right) & \dfrac{\partial v}{\partial y} & \dfrac{1}{2}\left(\dfrac{\partial v}{\partial z}+\xi\dfrac{\partial w}{\partial y}\right) \\[2mm] \dfrac{1}{2}\left(\dfrac{\partial u}{\partial z}+\xi\dfrac{\partial w}{\partial x}\right) & \dfrac{1}{2}\left(\dfrac{\partial v}{\partial z}+\xi\dfrac{\partial w}{\partial y}\right) & -\left(\dfrac{\partial u}{\partial x}+\dfrac{\partial v}{\partial y}\right) \end{bmatrix} \tag{26}$$

281 and, corresponding to (6), the modified viscosity,

$$\tilde{\mu}_n = \eta_0 \left(\tilde{\dot{\varepsilon}}^2\right)^{(1-n)/2n}, \tag{27}$$

283 is given in terms of the second invariant, $\tilde{\dot{\varepsilon}}^2 = \tilde{\dot{\varepsilon}}_{ij}\tilde{\dot{\varepsilon}}_{ij}/2$, that in expanded form becomes

$$\tilde{\dot{\varepsilon}}^2 = \left(\frac{\partial u}{\partial x}\right)^2 + \frac{\partial u}{\partial x}\frac{\partial v}{\partial y} + \left(\frac{\partial v}{\partial y}\right)^2 + \frac{1}{4}\left[\left(\frac{\partial u}{\partial y}+\frac{\partial v}{\partial x}\right)^2 + \left(\frac{\partial u}{\partial z}+\xi\frac{\partial w}{\partial x}\right)^2 + \left(\frac{\partial v}{\partial z}+\xi\frac{\partial w}{\partial y}\right)^2\right]. \tag{28}$$

285 Since (28) differs from (7) only by the use of the continuity equation (22), the

286 transformation will leave the second invariant $\tilde{\dot{\varepsilon}}^2$ and viscosity $\tilde{\mu}_n$ unchanged, i.e.,

287 $\tilde{\dot{\varepsilon}}^2 = \dot{\varepsilon}^2$ and $\tilde{\mu}_n = \mu_n$, and the transformed second invariant remains positive, i.e., $\tilde{\dot{\varepsilon}}^2 \geq 0$.

288

289   The dummy variables $\xi, \hat{\xi}$ in (23)-(25) and (26)-(29) are used to identify terms

290 that are neglected in the two types of the Blatter-Pattyn approximation discussed in §3.4.

291 These are (a) the standard Blatter-Pattyn approximation, $\xi = 0, \hat{\xi} = 0$, as originally

292 derived (Blatter, 1995; Pattyn, 2003; DPL, 2010), which solves for just the horizontal

293 velocity components, and (b) the extended Blatter-Pattyn approximation, $\xi = 0, \hat{\xi} = 1$,

294 described more fully later, that contains the standard approximation together with

October 15, 2024

295   additional equations that determine the vertical velocity w and the pressure $\tilde{P}$. Keeping

296   all terms, i.e., $\xi = 1, \hat{\xi} = 1$, specifies the full transformed Stokes model.

297

298   Boundary conditions for the transformed equations, corresponding to (8)-(11), are

299   given by

300   BCs on S_S: $\qquad\qquad\qquad\qquad \tilde{\tau}_{ij}n_j - \hat{\xi}\tilde{P}n_i = 0$, $\qquad\qquad\qquad\qquad$ (29)

301   BCs on S_{B1}: $\qquad\qquad\qquad\qquad\quad u_i = 0$, $\qquad\qquad\qquad\qquad\qquad$ (30)

302   BCs on S_{B2}: $\qquad\qquad\qquad\qquad\quad u_i n_i = 0$, $\qquad\qquad\qquad\qquad\qquad$ (31)

303 $\qquad\qquad\qquad\qquad \tilde{\tau}_{(i)j}n_j - \tilde{\tau}_n n_{(i)} + \beta(x)u_{(i)} = 0$, $\qquad\qquad\qquad$ (32)

304   where $\tilde{\tau}_n = n_i\tilde{\tau}_{ij}n_j$ as before. Equations (31), (32) constitute the three required boundary

305   conditions for frictional sliding.

306

307   The transformed system, (25)-(32), and the standard Stokes system, (2)-(11), yield

308   exactly the same solution. However, in common with the Blatter-Pattyn approximation,

309   transformation (21) needs to use a gravity-oriented coordinate system because of the

310   particular form of the gravitational forcing term, while the standard Stokes model does

311   not have this restriction. This is not a major limitation. A somewhat more restrictive

312   limitation is the appearance of $z_s(x,y)$, an implicitly single valued function, to describe

313   the vertical position of the upper surface of the ice sheet. This means that care must be

314   taken in case of reentrant upper surfaces (i.e., S-shaped in 2D) and sloping cliffs at the ice

315   edge, a restriction not present in the standard Stokes model. For simplicity, as noted

316   before we assume that there is just one upper and one basal surface. That is, as usual in

317   ice sheet modeling we do not permit overhangs.

318

319   **3.3 The Transformed Stokes Variational Principle**

320

321   It is easy to verify that the transformed Stokes system (23)-(32) results from the variation

322   with respect to $u_i, \tilde{P}$ of the following functional:

October 15, 2024

$$\tilde{\mathcal{A}}[u_i, \tilde{P}] = \int_V dV \left[\frac{4n}{n+1} \eta_0 \left(\tilde{\dot{\varepsilon}}^2 \right)^{(1+n)/2n} - \hat{\xi} \tilde{P} \frac{\partial u_i}{\partial x_i} + \rho g u_{(i)} \frac{\partial z_s}{\partial x_{(i)}} \right]$$
$$+ \frac{1}{2} \int_{S_{B2}} dS\, \beta(x) \left(u_{(i)} u_{(i)} + \left(u_{(i)} n_{(i)} / n_z \right)^2 \right), \tag{33}$$

where $\tilde{\dot{\varepsilon}}^2$ is the transformed second invariant from (28). Basal boundary conditions are imposed by direct substitution, as in (15). Alternatively, one could also impose boundary conditions using Lagrange multipliers as in (13), if desired.

3.4 Two Blatter-Pattyn Approximations
3.4.1 The Standard Blatter-Pattyn Approximation

The standard (or traditional) Blatter-Pattyn approximation (originally introduced by Blatter, 1995; Pattyn, 2003; later by DPL, 2010; Schoof and Hewitt, 2013, and references therein) is obtained by setting $\xi = 0, \hat{\xi} = 0$ in the transformed system. This yields the following Blatter-Pattyn variational functional,

$$\mathcal{A}_{BP}[u_{(i)}] = \int_V dV \left[\frac{4n}{n+1} \eta_0 \left(\dot{\varepsilon}_{BP}^2 \right)^{(1+n)/2n} + \rho g u_{(i)} \frac{\partial z_s}{\partial x_{(i)}} \right]$$
$$+ \frac{1}{2} \int_{S_{B2}} dS\, \beta(x) \left(u_{(i)} u_{(i)} + \varsigma \left(u_{(i)} n_{(i)} / n_z \right)^2 \right), \tag{34}$$

in terms of horizontal velocity components only, where the second invariant $\dot{\varepsilon}_{BP}^2$ follows from (28) with $\xi = 0$,

$$\dot{\varepsilon}_{BP}^2 = \left(\frac{\partial u}{\partial x} \right)^2 + \frac{\partial u}{\partial x} \frac{\partial v}{\partial y} + \left(\frac{\partial v}{\partial y} \right)^2 + \frac{1}{4} \left[\left(\frac{\partial u}{\partial y} + \frac{\partial v}{\partial x} \right)^2 + \frac{\partial u}{\partial z}^2 + \frac{\partial v}{\partial z}^2 \right], \tag{35}$$

and therefore the Euler-Lagrange equations and boundary conditions become

$$\frac{\partial \tau_{(i)j}^{BP}}{\partial x_j} - \rho g \frac{\partial z_s}{\partial x_{(i)}} = 0; \quad \begin{cases} \tau_{(i)j}^{BP} n_j + \beta(x) \left(u_{(i)} + \varsigma \left(u_{(j)} n_{(j)} / n_z \right) n_{(i)} / n_z \right) = 0 \\ \text{on } S_{B2}, \quad \tau_{(i)j}^{BP} n_j = 0 \text{ on } S_S, \quad u_{(i)} = 0 \text{ on } S_{B1}, \end{cases} \tag{36}$$

where the Blatter-Pattyn stress tensor $\tau_{(i)j}^{BP}$ is

October 15, 2024

$$342 \quad \tau_{(i)j}^{BP} = \eta_0 \left(\dot{\varepsilon}_{BP}^2 \right)^{(1-n)/2n} \begin{bmatrix} 2\left(2\dfrac{\partial u}{\partial x} + \dfrac{\partial v}{\partial y} \right) & \left(\dfrac{\partial u}{\partial y} + \dfrac{\partial v}{\partial x} \right) & \dfrac{\partial u}{\partial z} \\ \left(\dfrac{\partial u}{\partial y} + \dfrac{\partial v}{\partial x} \right) & 2\left(\dfrac{\partial u}{\partial x} + 2\dfrac{\partial v}{\partial y} \right) & \dfrac{\partial v}{\partial z} \end{bmatrix}. \quad (37)$$

343 These last two equations correspond to (23) and (25) in the transformed Stokes system.

344 There is a new dummy variable ζ in (34) introduced to identify the basal boundary term

345 normally dropped $(\zeta = 0)$ in the standard Blatter-Pattyn approximation but restored

346 $(\zeta = 1)$ in Dukowicz et al. (2011) to better deal with arbitrary basal topography.

347

348   The Blatter-Pattyn model is a well-behaved nonlinear approximate system for the

349 horizontal velocity components u, v because in this case the variational formulation is a

350 convex optimization problem whose solution minimizes the functional. As noted in the

351 Introduction, the Blatter-Pattyn approximation is widely used in practice as an

352 economical and relatively accurate ice sheet model. If desired, the vertical velocity

353 component w may be computed a posteriori by means of the continuity equation.

354

355 **Remark #1**: The original formulation (e.g., Pattyn, 2003) approximates the normal unit

356 vectors n_i on the frictional part of the basal boundary S_{B2} by making the small slope

357 approximation. However, this additional approximation is unnecessary since any

358 computational savings are negligible (Dukowicz et al., 2011; Perego et al., 2012).

359

360 **3.4.2 The Extended Blatter-Pattyn Approximation**

361

362 A second form of the Blatter-Pattyn approximation is obtained from the transformed

363 variational principle (33) by making the assumption,

$$364 \quad \left\| \dfrac{\partial w}{\partial x} \right\| \ll \left\| \dfrac{\partial u}{\partial z} \right\|, \quad \left\| \dfrac{\partial w}{\partial y} \right\| \ll \left\| \dfrac{\partial v}{\partial z} \right\|, \quad (38)$$

365 and therefore neglecting $\partial w/\partial x, \partial w/\partial y$ in the transformed second invariant $\tilde{\dot{\varepsilon}}^2$, or

366 equivalently, in the strain rate tensor $\tilde{\dot{\varepsilon}}_{ij}$ from (26), consistent with the original small

367 aspect ratio approximation (Blatter, 1995; Pattyn, 2003; DPL, 2010; Schoof and

368 Hindmarsh, 2008). This corresponds to setting $\xi = 0, \hat{\xi} = 1$ in the transformed Stokes

October 15, 2024

369   model. In other words, we neglect vertical velocity gradients but keep the pressure term.

370   This will be called the extended Blatter-Pattyn approximation (EBP) because, in contrast

371   to the standard Blatter-Pattyn approximation, all the variables, i.e., $u, v, w, \tilde{P}$, are retained.

372   Notably, assumption (38) is equivalent to just setting $w = 0$ in the second invariant $\tilde{\dot{\varepsilon}}^2$ in

373   the full transformed Stokes model. That is, the extended BP approximation is obtained

374   by neglecting vertical velocities everywhere in (33) except where they occurs in the

375   velocity divergence term. This aspect of the transformed Stokes model will be exploited

376   later to obtain approximations that improve on Blatter-Pattyn. Thus, the extended

377   Blatter-Pattyn functional is given by

378
$$\mathcal{A}_{EBP}[u_i, \tilde{P}] = \int_V dV \left[\frac{4n}{n+1} \eta_0 \left(\dot{\varepsilon}_{BP}^2 \right)^{(1+n)/2n} - \tilde{P} \frac{\partial u_i}{\partial x_i} + \rho g u_{(i)} \frac{\partial z_s}{\partial x_{(i)}} \right]$$
$$+ \frac{1}{2} \int_{S_{B2}} dS \, \beta(x) \left(u_{(i)} u_{(i)} + \varsigma \left(u_{(i)} n_{(i)} / n_z \right)^2 \right), \tag{39}$$

379   and the Blatter-Pattyn second invariant $\dot{\varepsilon}_{BP}^2$ is given by (35). Taking the variation of the

380   functional, the system of extended Blatter-Pattyn Euler-Lagrange equations and their

381   boundary conditions is given by

382   (1) Variation with respect to $u_{(i)}$ yields the horizontal momentum equation:

383
$$\frac{\partial \tau_{(i)j}^{BP}}{\partial x_j} - \frac{\partial \tilde{P}}{\partial x_{(i)}} - \rho g \frac{\partial z_s}{\partial x_{(i)}} = 0; \quad \left\{ \begin{array}{l} \tau_{(i)j}^{BP} n_j - \tilde{P} n_{(i)} = 0 \text{ on } S_S, \quad u_{(i)} = 0 \text{ on } S_{B1}, \\ \tau_{(i)j}^{BP} n_j + \beta(x) \left(u_{(i)} + \zeta \left(u_{(k)} n_{(k)} / n_z \right) n_{(i)} / n_z \right) = 0 \\ \text{ on } S_{B2}, \end{array} \right. \tag{40}$$

384   where $\tau_{(i)j}^{BP}$ is given by (37).

385   (2) Variation with respect to w yields the vertical momentum equation:

386
$$-\frac{\partial \tilde{P}}{\partial z} = 0; \qquad \tilde{P} n_z = 0 \text{ on } S_S, \tag{41}$$

387   (3) Variation with respect to $\tilde{P}$ yields the continuity equation:

388
$$\frac{\partial w}{\partial z} + \frac{\partial u_{(i)}}{\partial x_{(i)}} = 0; \quad w = 0 \text{ on } S_{B1}, \text{ or } w = -u_{(i)} n_{(i)} / n_z \text{ on } S_{B2}. \tag{42}$$

389   It is apparent that the vertical momentum equation system (41) is decoupled, yielding

390     $\tilde{P} = 0$, as was already shown in §3.1. This eliminates pressure from the horizontal

391   momentum equation (40), making it a decoupled equation for the horizontal velocities

392     $u_{(i)}$, identical to the standard Blatter-Pattyn system (36). In addition, having obtained the

393   horizontal velocities from (40), the continuity equation (42) may now be solved for the

394   vertical velocity w (but see the comments regarding the discrete case that follow (43)).

395

396   In summary, the extended Blatter-Pattyn model, (40)-(42), is equivalent to the

397   standard Blatter-Pattyn model, (36), for the horizontal velocities, u, v, except that it also

398   includes two additional equations that determine the pressure $\tilde{P}$ and the vertical velocity

399   w that are usually ignored in the standard Blatter-Pattyn approximation where only the

400   horizontal velocity is calculated. Because of this, we distinguish between the _Blatter-_

401   _Pattyn model_ that solves for just the two horizontal velocities (i.e., the standard Blatter-

402   Pattyn approximation, (36)), and the _Blatter-Pattyn system_ that solves for all the variables

403   (i.e., the extended Blatter-Pattyn approximation, (40)-(42)). Perhaps the main distinction

404   between the two is that the Blatter-Pattyn system obtains the vertical velocity on the same

405   grid as the horizontal velocities, while the calculation of vertical velocity in the Blatter-

406   Pattyn model is completely decoupled and may be done on an unrelated grid. These

407   models must obtain the vertical velocity w from the continuity equation (42) once

408   horizontal velocities u, v are available. In the continuous case this may be done using

409   Leibniz's theorem, as follows

410
$$w(u,v) = w_{z=z_b} - \int_{z_b}^{z} \frac{\partial u_{(i)}}{\partial x_{(i)}} dz' = u_{(i)} \frac{\partial z_b}{\partial x_{(i)}} - \int_{z_b}^{z} \frac{\partial u_{(i)}}{\partial x_{(i)}} dz' = -\frac{\partial}{\partial x_{(i)}} \int_{z_b}^{z} u_{(i)} dz'. \qquad (43)$$

411   In the discrete case $w(u,w)$ may be obtained by directly discretizing (43). Later we shall

412   consider special finite element grids where the continuity equation is invertible so as to

413   obtain w.

414

415   So far we have only considered continuum properties of Stokes-type systems.

416   However, a discrete finite element formulation may not be well behaved. The solution of

417   discretized Stokes models and Blatter-Pattyn approximations, and the solution for vertical

418   velocity from the continuity equation will depend on the choices made for the grids and

419   the finite elements that are to be used. These issues will be discussed next.

420

October 15, 2024

421 **4. Finite Element Discretization**

422 **4.1 Standard and Transformed Stokes Discretizations**

423

424 In practice, both traditional Stokes and Blatter-Pattyn models are discretized using finite

425 element methods (e.g., Gagliardini et al., 2013; Perego et al., 2012). We follow this

426 practice except that here the discretization originates from a variational principle. This

427 has a number of advantages (see §2.3 and DPL, 2010). The following is a brief outline of

428 the finite element discretization. Additional details about the grid and the associated

429 discretization are provided in Appendix B. For simplicity, we confine ourselves to two

430 dimensions with coordinates (x,z) and velocities (u,w). Generalization to three

431 dimensions is possible (an example of a three-dimensional grid appropriate for our

432 purpose is discussed in Appendix B). Further, we discuss only the case of direct

433 substitution for basal boundary conditions in the variational functional, i.e., (15) or (33).

434 The remarks in this Section will apply to both the standard and transformed Stokes

435 models; for example, the discrete pressure variable p may refer to either the standard

436 pressure P or the transformed pressure $\tilde{P}$.

437

438 Consider an arbitrary grid with a total of $N = n_u + n_w + n_p$ unknown discrete

439 variables at appropriate nodal locations $1 \le i \le N$, with n_u horizontal velocity variables,

440 n_w vertical velocity variables, and n_p pressure variables, so that

441 $$V = \left\{V_1, V_2, \cdots, V_N\right\}^T = \left\{\left\{u_1, u_2, \cdots, u_{n_u}\right\}, \left\{w_1, w_2, \cdots, w_{n_w}\right\}, \left\{p_1, p_2, \cdots, p_{n_w}\right\}\right\}^T = \left\{u, w, p\right\}^T \quad (44)$$

442 is the vector of all the unknown discrete variables that are the degrees of freedom of the

443 model. If using Lagrange multipliers for basal boundary conditions then discrete

444 variables corresponding to λ_z, Λ must be added. Variables are expanded in terms of

445 shape functions $N_i^k(\mathbf{x})$ associated with each nodal variable i in each element k, so that

446 $V^k(\mathbf{x}) = \sum_i V_i N_i^k(\mathbf{x})$ is the spatial variation of all variables in element k, summed over

447 all variable nodes located in element k. Shape functions associated with a given node

448 may differ depending on the variable (i.e., $u, w,$ or p). Substituting into the functional,

449 (15) or (33), integrating and assembling the contributions of all elements, we obtain a

450 discretized variational functional in terms of the nodal variable vectors u, w, p, as follows

October 15, 2024

$$\mathcal{A}(u,w,p) = \sum_k \mathcal{A}^k(u,w,p), \tag{45}$$

451

452 where $\mathcal{A}^k(u,w,p)$ is the local functional evaluated by integrating over element k. Since
453 the term in the functional involving the product of pressure and divergence of velocity is
454 linear in pressure and velocity, and the term responsible for gravity forcing is linear in
455 velocity, the functional (45) may be written in matrix form as follows

$$\mathcal{A}(u,w,p) = \mathcal{M}(u,w) + p^T\left(M_{UP}^T u + M_{WP}^T w\right) + u^T F_U + w^T F_W, \tag{46}$$

456

457 where the notation from (44) has been used, i.e., $u = \left\{u_1, u_2, \cdots, u_{n_u}\right\}^T$, etc. Parentheses
458 indicate a functional dependence on the indicated variables. Comparison with (15) and
459 (33) indicates that $\mathcal{M}(u,w)$ is a nonlinear positive-definite function of the velocity
460 components u, w, M_{UP}^T, M_{WP}^T are constant $n_p \times n_u$ and $n_p \times n_w$ matrices, respectively,
461 arising from the incompressibility constraint, and F_U, F_W are constant gravity forcing
462 vectors, of dimension n_u and n_w, respectively. Note that $F_U = 0, F_W \neq 0$ specifies the
463 standard Stokes model, and $F_U \neq 0, F_W = 0$ the transformed Stokes model. The discrete
464 functional $\mathcal{M}(u,w)$ differs but it remains positive-definite in both.
465
466   Discrete variation of the functional corresponds to partial differentiation with
467 respect to each of the discrete variables in V. Thus, the discrete Euler-Lagrange
468 equations that correspond to the u-momentum, w-momentum, and continuity equations,
469 respectively, are given by

$$R(u,w,p) = \begin{bmatrix} R_U(u,w,p) \\ R_W(u,w,p) \\ R_P(u,w) \end{bmatrix} = \begin{bmatrix} \mathcal{M}_U(u,w) + M_{UP}p + F_U \\ \mathcal{M}_W(u,w) + M_{WP}p + F_W \\ M_{UP}^T u + M_{WP}^T w \end{bmatrix} = 0, \tag{47}$$

470

471 where $R(u,w,p)$ is the residual vector with components $R_U(u,w,p) = \partial\mathcal{A}/\partial u$,
472 $R_W(u,w,p) = \partial\mathcal{A}/\partial w$, and $R_P(u,w) = \partial\mathcal{A}/\partial p$. The functionals $\mathcal{M}_U(u,w) = \partial\mathcal{M}/\partial u$,
473 $\mathcal{M}_W(u,w) = \partial\mathcal{M}/\partial w$ are nonlinear vectors of dimension n_u and n_w, respectively.
474 Altogether, (47) is a set of N equations for the N unknown discrete variables V_i. As

475 explained previously, all boundary conditions are already included in functional (46), and
476 therefore are also incorporated into the discrete Euler-Lagrange equations (47).
477
478   Since the overall system (47) is nonlinear, it is typically solved using Newton-
479 Raphson iteration, expressed in matrix notation as follows

$$M\left(u^{K},w^{K}\right)\Delta V + R\left(u^{K},w^{K},p^{K}\right)=0 , \qquad (48)$$

481 where K is the iteration index, $M(u,v)=\partial^{2}\mathcal{A}(V)/\partial V_{i}\,\partial V_{j}$ is a symmetric $N\times N$
482 Hessian matrix, and ΔV is the column vector given by

$$\Delta V = \left\{\Delta u,\Delta w,\Delta p\right\}^{T} = \left\{u^{K+1}-u^{K},w^{K+1}-w^{K},p^{K+1}-p^{K}\right\}^{T} .$$

484 Given V^{K} from the previous iteration, (48) is a linear matrix equation that is solved at
485 each iteration for the N new variables V^{K+1}. In view of (46) and (47), the Hessian
486 matrix $M(u,w)$ may be decomposed into several submatrices, as follows

$$M(u,w)=\begin{bmatrix} M_{UU}(u,w) & M_{UW}(u,w) & M_{UP} \\ M_{UW}^{T}(u,w) & M_{WW}(u,w) & M_{WP} \\ M_{UP}^{T} & M_{WP}^{T} & 0 \end{bmatrix}. \qquad (49)$$

488 Submatrices $M_{UW}(u,w)=\partial^{2}\mathcal{M}/\partial u\,\partial w$, etc., depend nonlinearly on u,w. Thus,
489 $M_{UU}(u,w), M_{WW}(u,w)$ are square $n_{u}\times n_{u}$, $n_{w}\times n_{w}$ symmetric matrices, respectively,
490 while $M_{UW}(u,w)$ is a rectangular $n_{u}\times n_{w}$ matrix since n_{u}, n_{w} may not be equal. As noted
491 earlier, M_{WP}^{T} is an $n_{p}\times n_{w}$ matrix and therefore not square unless $n_{p}=n_{w}$.
492

493 **4.2 Blatter-Pattyn Discretizations**
494

495 For completeness, we express the Blatter-Pattyn approximations from §3.4 in matrix
496 form, as follows
497   (1) The standard Blatter-Pattyn model from §3.4.1 takes the simple form

$$R^{BP}(u)= \mathcal{M}_{U}(u,0)+ F_{U} =0 , \qquad (50)$$

499 whose Newton-Raphson iteration is given by

$$M^{BP}\left(u^{K}\right)\Delta u+ R^{BP}\left(u^{K}\right)=0 , \qquad (51)$$

October 15, 2024

501   and therefore the Blatter-Pattyn Hessian matrix is given by $M^{BP}(u) = M_{UU}(u,0)$.

502   (2) The extended Blatter-Pattyn approximation from §3.4.2 becomes

503
$$R^{EBP}(u,w,p) = \begin{bmatrix} \mathcal{M}_U(u,0) + M_{UP}p + F_U \\ M_{WP}p \\ M_{UP}^T u + M_{WP}^T w \end{bmatrix} = 0 ,$$
(52)

504   with the Newton-Raphson iteration given by

505
$$M^{EBP}(u^K)\Delta U^{K+1} + R^{EBP}(u^K, w^K, p^K) = 0 ,$$
(53)

506   and where the associated Hessian matrix is

507
$$M^{EBP}(u) = \begin{bmatrix} M_{UU}(u,0) & 0 & M_{UP} \\ 0 & 0 & M_{WP} \\ M_{UP}^T & M_{WP}^T & 0 \end{bmatrix} .$$
(54)

508

509   **4.3 Solvability Issues**

510   **4.3.1 Solvability of Stokes and Blatter-Pattyn Models**

511

512   We now consider the solution of the three linear matrix problems (48), (51), (53)

513   associated with the Stokes and the corresponding Blatter-Pattyn approximate models.

514   While there are no issues in the continuous case, this is not so in the discrete case

515   depending on the choice of the grid and the finite elements, as noted earlier. The discrete

516   system to be solved has the general form

517
$$\mathbf{M}\begin{Bmatrix} \mathbf{u} \\ p \end{Bmatrix} = \begin{bmatrix} A & B \\ B^T & 0 \end{bmatrix}\begin{Bmatrix} \mathbf{u} \\ p \end{Bmatrix} = \begin{Bmatrix} \mathbf{f} \\ g \end{Bmatrix} ,$$
(55)

518   where $\mathbf{u} = \{u,w\}^T$ in the linear case or $\{\Delta u, \Delta w\}^T$ in the nonlinear case, and similarly for

519   the vector of pressures or pressure increments p. The form (55) is characteristic of

520   Stokes-type problems, or more generally of constrained minimization problems using

521   Lagrange multipliers. In finite element terminology these are called "mixed" or "saddle

522   point" problems, meaning that velocity components and the pressure occupy different

523   finite element spaces, and that the solution of (55) is actually at the saddle point with

524   respect to the velocity and pressure variables of the quadratic form associated with (55).

525   The matrix $\mathbf{M}$ is symmetric but indefinite, with both positive and negative eigenvalues.

526   As a result, the matrix inverse may not be bounded and may lack stability.

October 15, 2024

527

528   There are three cases to consider:

529   (1) The standard Blatter-Pattyn model, (51). In this case only the matrix A

530   exists, it is elliptic, and $B = B^T = 0$. As a result, the standard Blatter-Pattyn model is a

531   well-behaved and stable unconstrained minimization problem. The model (51) is self-

532   contained and is solved for u while the vertical velocity w is potentially available a

533   posteriori from a separately obtained continuity equation.

534   (2) The extended Blatter-Pattyn model, (53), (54). The middle row of the Hessian

535   (54) indicates that the solution for the pressure will be zero. Using this in the top row of

536   the Hessian, one obtains the standard Blatter-Pattyn system and therefore the same well-

537   behaved horizontal velocity u as above, with the result that the bottom row of the

538   Hessian, the continuity equation, is the only way to obtain a solution for the vertical

539   velocity w. However, this is possible only if matrix M_{WP}^T is invertible, which at

540   minimum requires a square matrix, i.e., $n_p = n_w$, and this depends on the finite element

541   grid chosen for the discretization. For example, the popular second-order Taylor-Hood

542   (P2-P1) element with piecewise quadratic velocity and linear pressure (Hood and Taylor,

543   1973) typically has $n_p \ll n_w$. As a result, the linear system for w is greatly

544   underdetermined and cannot be solved for w. In fact, this is a problem for all inf-sup

545   stable elements with $n_p \neq n_w$, such as the Taylor-Hood element, for example.

546   (3) The standard and transformed Stokes models, (48), (49). These models

547   require the use of pressure as a Lagrange multiplier to enforce incompressibility and

548   therefore these are mixed or saddle point problems, as mentioned previously. To avoid

549   problems with the solution these finite elements must satisfy a certain condition, the

550   Ladyzhenskaya–Babuška–Brezzi (LBB, or inf-sup) condition. There is a very large

551   literature on the subject, e.g., Boffi et al. (2008), Elman et al. (2014), Auricchio et al.

552   (2017). Both the standard and transformed Stokes models are subject to this problem and

553   in general must use inf-sup stable finite elements. Testing for stability is not trivial.

554   However, collections of inf-sup stable elements for the Stokes equations may be found in

555   many papers and books on mixed methods, e.g., Boffi et al. (2008). The popular second-

556   order Taylor-Hood P2-P1 element (Hood and Taylor, 1973) is an example of an inf-sup

557   stable element. Some results involving this element are shown in Fig. 13 for Test B, one

558   of the test problems described in Appendix A.

559

October 15, 2024

4.3.2 A Special Case: Invertible Continuity Equation

In the continuous case, the Blatter-Pattyn approximation (§3.4.1) implies that vertical velocity w is obtainable from the continuity equation after having solved for the horizontal velocities u, v. As mentioned previously, this is possible to do in the continuum but not necessarily so in the discrete case. The 2D discrete continuity equation from (47) or (52) is given by

$$M_{UP}^T u + M_{WP}^T w = 0 . \tag{56}$$

For this to be solvable for w in terms of the horizontal velocity, i.e., $w(u)$, means that matrix M_{WP}^T must be invertible and thus it must be square and full rank. Since in general M_{WP}^T is an $n_p \times n_w$ matrix, for solvability at minimum this requires that

$$n_p = n_w . \tag{57}$$

Assuming that we are dealing with reasonable discretizations, we shall presume for our discussion that matrix M_{WP}^T is always full rank. If Lagrange multipliers were to be used, this means that the number of unknown pressures n_p would have to be augmented by the number of Lagrange multipliers so (57) would become $n_p + \lambda_z + \Lambda = n_w$ (See Appendix B, §B2, for more details). We shall refer to (57) (together with the assumption of full rank) as the solvability condition. In Appendix B we present several grids and elements that satisfy this condition, including one variant in particular, the P1-E0 element, that will be used in most of the 2D test problems featured in this paper. Thus, if the solvability condition is satisfied, the discrete continuity equation (56) may be inverted for the vertical velocity, to obtain

$$w(u) = -M_{WP}^{-T} M_{UP}^T u , \tag{58}$$

where matrix M_{WP}^{-T} is defined by

$$M_{WP}^{-T} = \left(M_{WP}^T \right)^{-1} = \left(M_{WP}^{-1} \right)^T . \tag{59}$$

Here wee have used the fact that if matrix M_{WP}^T is invertible then so is its transpose M_{WP}. Note that (58) is one discrete form of equation (43).

Invertibility of the continuity equation has several important applications. First, it is a necessary requirement for the new Stokes approximations that are discussed in §6.2.

October 15, 2024

590   Since these approximations are based on approximating the vertical velocity in the

591   transformed second invariant, (28), it is necessary to obtain the vertical velocity

592   independently of solving the entire coupled Stokes problem. Second, we noticed earlier

593   that the extended Blatter-Pattyn model does not work with a Taylor-Hood P2-P1 grid

594   because the solvability condition is not satisfied. However, this model does work with a

595   variant of the Taylor-Hood grid, the P2-E1 grid, illustrated in Fig. 13A, which does

596   satisfy the solvability condition and this therefore allows for a successful calculation of

597   the vertical velocity.

598

599   Perhaps the main reason for the importance of the solvability condition is that it

600   implies that the Stokes variational principle, (15) or (33), may be transformed into and

601   therefore that it is equivalent to an optimization or minimization problem. Consider the

602   discrete form of the variational functional given by (46). Working with a grid that

603   satisfies the solvability condition, we may substitute the vertical velocity given by (58)

604   into the functional (46). This immediately eliminates the term responsible for the

605   continuity equation, including the pressure, and one obtains a functional in terms of

606   horizontal velocity u only, as follows

607
$$\mathcal{A}(u) = \mathcal{M}(u, w(u)) + u^T F_U + w(u)^T F_W. \tag{60}$$

608   Since the functional $\mathcal{M}(u, w(u))$ is positive semi-definite, this is now an unconstrained

609   minimization problem, entirely analogous to the standard Blatter-Pattyn problem of

610   §3.4.1 except that here it represents the full Stokes problem for either the standard (F_W)

611   or the transformed (F_U) formulation. This result suggests that a conventional Stokes

612   problem, when solved on a grid satisfying the solvability condition, is equivalent to an

613   unconstrained minimization problem and therefore is well behaved. This is because any

614   problem will give the same answer whether formulated as (46) or (60) on a grid that

615   satisfies the solvability condition.

616

617   An equivalent point of view is presented in Boffi et al. (2008) who point out that

618   if a divergence-free basis exists then the Stokes problem becomes "a standard

619   minimization problem and the discrete form would lead to a positive definite linear

620   system", i.e., (60). The divergence-free basis in this case is given by $\{u, w(u)\}$.

621

October 15, 2024

622   **Remark #2**: Functional (60) is actually the discrete version of a pressure-free

623   formulation that was attempted analytically by Dukowicz (2012). It is possible to solve

624   problems using the pressure-free formulation (60) instead of a standard saddle point

625   formulation such as (46) or (47). However, this produces a dense Hessian matrix that

626   makes a solution using Newton-Raphson iteration very costly and therefore impractical,

627   particularly for large problems.

628

629   **5. Comparison of the Standard and Transformed Stokes Models**

630

631   The standard and transformed Stokes models are expected to converge to the same

632   solution. To verify that this is indeed the case we do a number of calculations for some

633   2D test problems based on the ISMIP-HOM benchmark (Pattyn et al, 2008). These tests

634   are described in Appendix A where they are referred to as Test B and Test D*. Test B

635   involves no-slip boundary conditions on a sinusoidal bed, and Test D* evaluates sliding

636   of the ice sheet along a flat bed in the presence of sinusoidal friction. The tests are

637   discretized using P1-E0 elements on a regular grid composed of n quadrilaterals in the x

638   -direction and m quadrilaterals in the z-direction, illustrated in Fig. B1, with each

639   quadrilateral divided into two triangles. Results are presented for two domain lengths,

640    $L = 5$ km and 10 km, to test the aspect ratio range where the Blatter-Pattyn model begins

641   to fail, and using a relatively coarse grid, i.e., $m = n = 40$, except when we consider the

642   convergence of the models with grid refinement in Fig. 3.

643
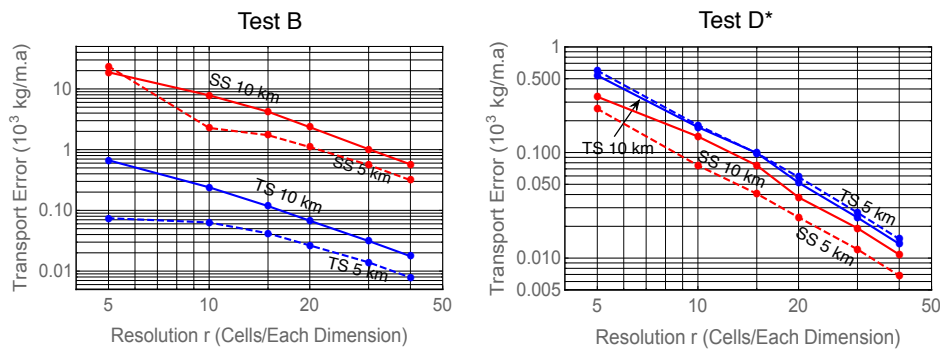
644   **Figure 3.** Convergence of ice transport in Tests B and D* with grid refinement.

645   Transformed Stokes (TS) plots are in blue and standard Stokes plots (SS) are in red.

646

647   Fig. 3 evaluates the convergence of the two Stokes models as a function of grid

648   resolution r, where r is the number of quadrilaterals in either direction. The models do

649   converge to the same solution and convergence is second order as expected from the use

650   of linear elements. Interestingly, the transformed Stokes model displays considerably

651   smaller error at all resolutions in Test B. As a result, the standard Stokes calculations are

652   not fully converged even at the 40x40 resolution. Fig. 4 shows the vertical profiles of the

653   horizontal velocity u at outflow, $x = L$. We plot results from the no-slip Test B problem

654   and the two frictional sliding problems, Tests D and D*. The Test D profile from the

655   ISMIP-HOM benchmark is almost vertically constant, indicating that the value for basal

656   friction originally chosen is too small. This emotivated the change from Test D to Test

657   D* in Appendix A.

658
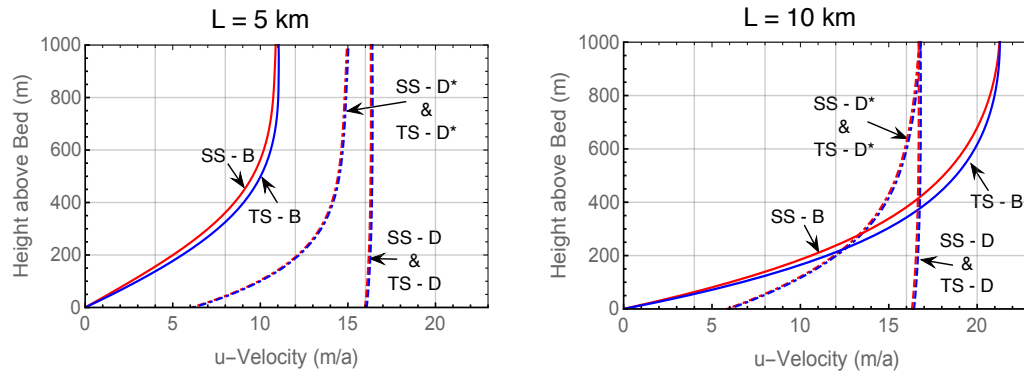
659   **Figure 4.** The u-velocity profile at location $x = L$ as a function of height from the bed.

660

661   Figs. 5 and 6 show the u-velocity at the ice sheet upper surface for Tests B and

662   D*. This is the benchmark used in ISMIP-HOM to compare the different ice sheet

663   models. Here we compare four cases: the standard Stokes model (SS), the transformed

664   Stokes model (TS), the Blatter-Pattyn (BP) model, and for reference, a very high

665   resolution full-Stokes Test B calculation "oga1" (SS-HR), available from the ISMIP-

666   HOM paper and also independently available in Gagliardini and Zwinger (2008). The TS

667   and the SS-HR plots lie on top of one another (they have been offset slightly for clarity),

668   indicating that the TS model is already fully converged. We again observe that the SS

669   model is not yet converged in Test B, particularly at $L = 5$ km. As also seen in the

670   ISMIP-HOM paper, the Blatter-Pattyn calculation (BP) shows large deviations from the

671   Stokes results, especially so at $L = 5$ km where the surface velocity is entirely out of

672   phase with the Stokes results. Test D* results in Fig. 6 for the SS and TS models are very

673   similar (the SS plot has been slightly offset upward for visibility). As expected, the error

674   in the Blatter-Pattyn results is noticeable at $L = 10$ km and very large at $L = 5$ km.

675   Pressures calculated on the P1-E0 grid are particularly smooth and well behaved but they

676   are not shown because pressure has little or no physical significance, particularly in the

677   transformed case.

October 15, 2024

678
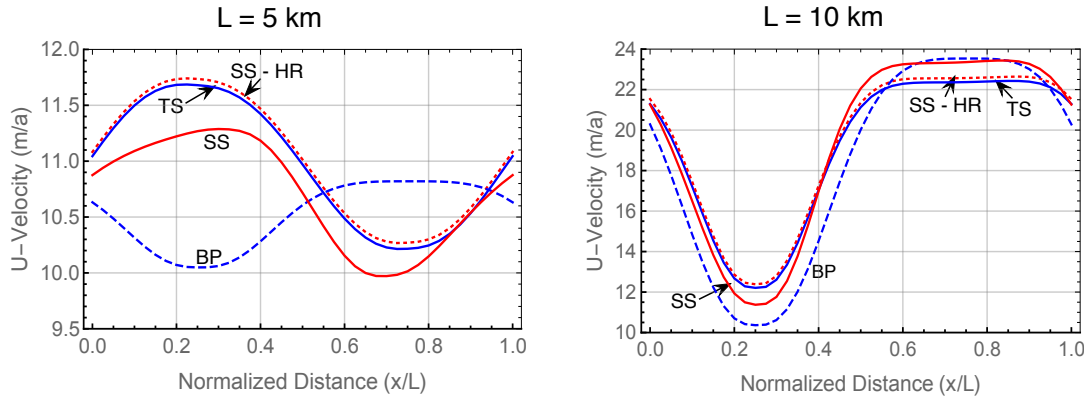
679 **Figure 5.** Upper surface u-velocity, $u(x,z_s)$ - Test B, No-slip boundary conditions.

680

681
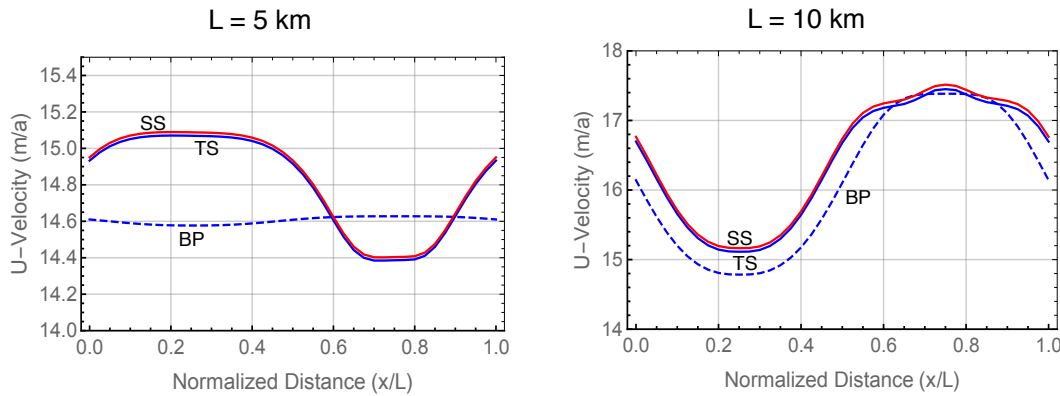
682 **Figure 6.** Upper surface u-velocity, $u(x,z_s)$ - Test D*, Modified frictional sliding.

683

684 **6. Applications of the Transformed Stokes Model**

685 **6.1 Adaptive Switching between Stokes and Blatter-Pattyn Models**

686

687 One way of reducing the cost of a full Stokes calculation is to use it adaptively with a

688 cheaper approximate model. That is, one may use the cheaper model in those parts of a

689 problem where it is accurate, and the more expensive full Stokes model where the

690 approximate model loses accuracy. One example of such an adaptive approach is the

691 tiling method by Seroussi et al. (2012). However, there are drawbacks to such methods,

692 such as the difficulty of incorporating two or more presumably quite different models

693 into a single model, and the additional complexity of a necessary transition zone to

694 couple the disparate models.

695

696   The transformed Stokes model used in such an adaptive role is attractive because

697 it may be switched between the Stokes and Blatter-Pattyn cases simply by switching the

October 15, 2024

698 parameter $\xi \in \{0,1\}$ between its two values. For simplicity the extended Blatter-Pattyn

699 approximation ($\xi = 0, \hat{\xi} = 1$) is being used since both the Stokes and the Blatter-Pattyn

700 parts of the code have the same number of discrete variables. The extended Blatter-

701 Pattyn model requires the use of a grid that satisfies the solvability condition as explained

702 in §4.3. We therefore use the P1-E0 element. It would be computationally cheaper to

703 use the standard Blatter-Pattyn approximation ($\xi, \hat{\xi} = 0$) instead, solving only for the

704 horizontal variables and coupling to the Stokes model with $p = 0$ and $w = w(u,v)$ at the

705 interface but this, however, implies much more complicated programming.

706

707   To demonstrate the idea of adaptive switching with a transformed Stokes model,

708 we introduce a new problem, Test O, described in Appendix A and illustrated in Fig. A1.

709 This consists of an inclined ice slab whose movement is obstructed by a thin obstacle

710 protruding 20% of the ice depth up from the bed. No-slip boundary conditions are

711 applied along the bed and on the obstacle itself. Because of the localized nature of the

712 obstacle, the Blatter-Pattyn approximation conditions, (38), must fail near the obstacle

713 and therefore the full Stokes model is needed for good accuracy, at least locally.

714
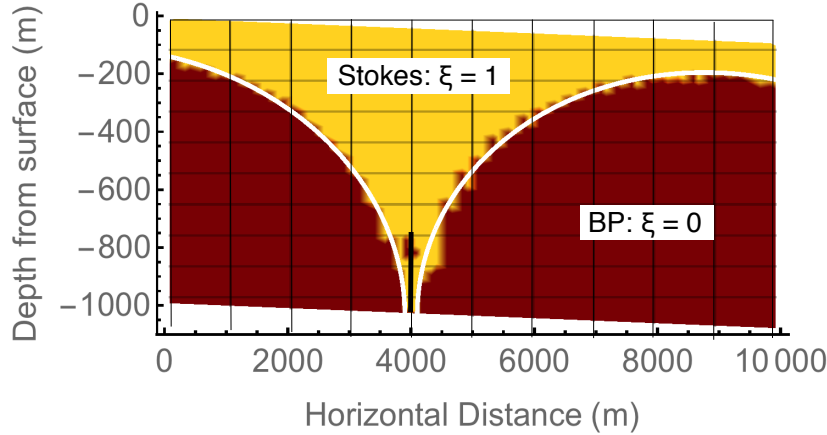
715 **Figure 7.** Mask function (white curve, $z = F_M(x)$) to indicate where the Stokes and BP

716 models are activated in the 20% obstacle test problem. The dark brown region delineates

717   the region where $|\partial w/\partial x| \leq 0.1|\partial u/\partial z|$ in a Blatter-Pattyn calculation.

718

719   To implement this, we first use a Blatter-Pattyn calculation to outline regions

720 where $|\partial w/\partial x| \leq 0.1|\partial u/\partial z|$, approximately localizing where the Blatter-Pattyn

October 15, 2024

721 approximation is valid. This determines a mask function $z = F_M(x)$, illustrated in Fig. 7

722 by the white curves, that specifies where the two models must be used. Defining the

723 centroid of a triangular element by (x_C, z_C), the code makes a selection in each element:

724
$$z_C \leq F_M(x_C) \quad \Rightarrow \quad \text{Set } \xi = 0, \quad \text{i.e., the Blatter-Pattyn region,}$$
$$z_C > F_M(x_C) \quad \Rightarrow \quad \text{Set } \xi = 1, \quad \text{i.e., the Stokes region.}$$

725 Somewhat counterintuitively, the Stokes region occupies the upper part of the domain in

726 Fig. 7 and includes the obstacle, while the Blatter-Pattyn region occupies much of the

727 bottom part of the domain. A transition zone, e.g., $0 \leq \xi(x,z) \leq 1$, is possible but was not

728 used in the present calculation.
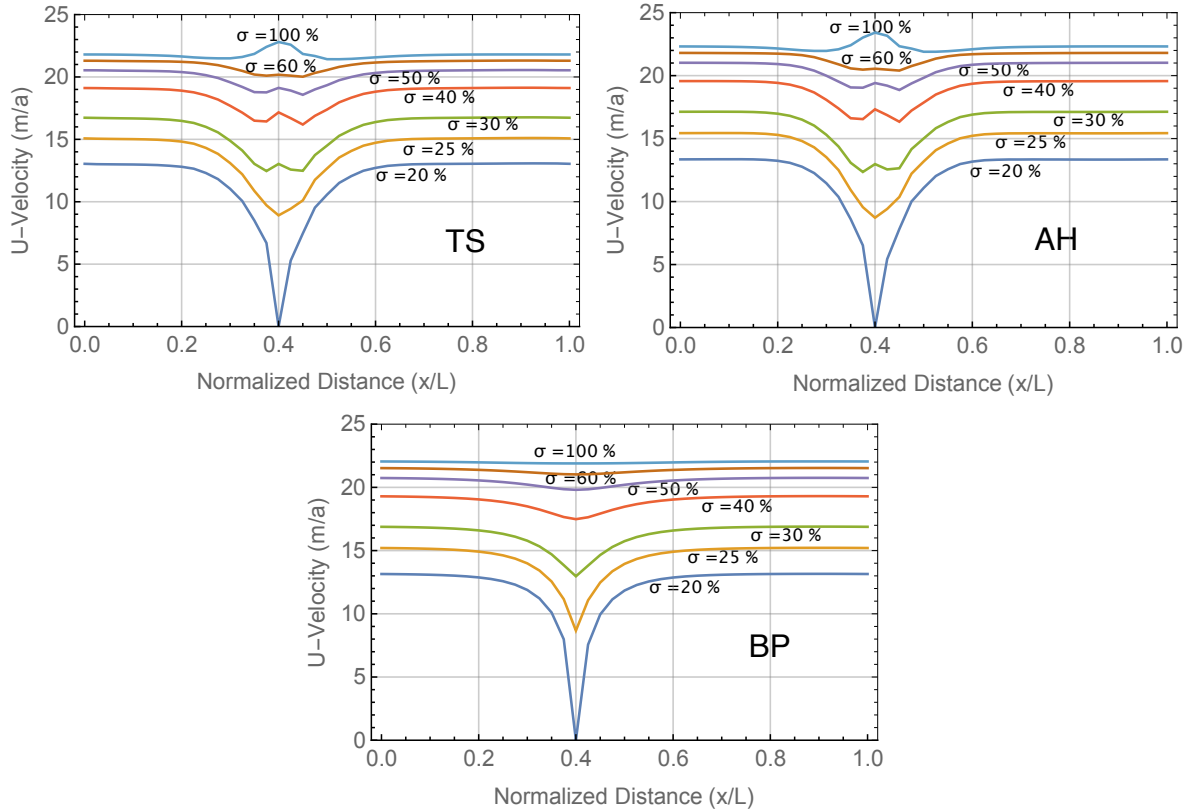
729
730 **Figure 8.** Comparing results for the Transformed Stokes (TS),
731   the Adaptive-Hybrid (AH), and the Blatter-Pattyn (BP) models in Test O.
732

733   The Adaptive-Hybrid results are shown in Fig. 8, which shows curves of the

734 horizontal velocity u at seven different vertical positions specified as a percentage of the

735 distance between top and bottom, with $\sigma = 100\%$ at the top surface. The top right panel

736 shows the results for the adaptive-hybrid model (AH). For comparison, the top left panel

October 15, 2024

737 and the bottom panel show results for the Stokes (TS) and the Blatter-Pattyn (BP)

738 calculations, respectively. All calculations are at the 40x40 resolution. The Adaptive-

739 Hybrid results are very similar to the full Stokes results, reproducing most features of the

740 velocity profiles, including the velocity bump at the top surface, indicating that even the

741 top surface feels the presence of the obstacle. The Blatter-Pattyn results are much less

742 accurate; they completely miss the details of the flow near the obstacle. We also measure

743 the RMS error in the u-velocity relative to the Stokes results. The RMS error in the

744 Blatter-Pattyn case is 0.493 m/a and 0.440 m/a in the Adaptive-Hybrid case, smaller in

745 the Blatter-Pattyn case as expected, but the difference is not as large and striking as the

746 visual difference in Fig. 8. Nevertheless, the adaptive-hybrid method is successful

747 judged by the Fig. 8 results alone. Unfortunately, an estimate of the computational cost

748 savings will have to wait a more realistic implementation.

749

750 **6.2. Two Stokes Approximations Beyond Blatter-Pattyn**

751

752 As shown in §3.4, simply setting $w = 0$ in the second invariant $\tilde{\varepsilon}^2$ in the transformed

753 functional $\tilde{\mathcal{A}}$ results in the standard Blatter-Pattyn approximation. This suggests that

754 approximating the vertical velocity w in the functional would be a good way to create

755 approximations that improve on the Blatter-Pattyn approximation since $w = 0$ already

756 produces an excellent approximation. We will look at two such methods in this Section

757 although others are possible. The first method, to be called the BP+ approximation, is

758 implemented using a combination of Newton and Picard iterations such that at each

759 Newton iteration the pressure-free variational functional is evaluated using a lagged

760 vertical velocity w^K from the previous iteration. The pressure is used in a subordinate

761 role as a "test function" to obtain a decoupled invertible continuity equation to obtain

762 $w(u^K)$. Although this method improves on the accuracy of the Blatter-Pattyn

763 approximation, its overall accuracy is limited because it uses only the horizontal

764 momentum equation and neglects the vertical momentum equation. The second method,

765 to be called the Dual-Grid approximation, keeps the pressure and vertical velocity as in

766 the transformed Stokes model but approximates it by discretizing the continuity equation

767 on a coarser grid. Since vertical velocity w is determined by inverting the continuity

768 equation, this has the effect of approximating the vertical velocity while reducing the

769 number of pressure and vertical velocity variables. This preserves the structure of the

October 15, 2024

770 Stokes model, while the degree of approximation is determined by the amount of

771 coarsening of the continuity grid.

772

773 **6.2.1 An Improved Blatter-Pattyn or BP+ Approximation**

774

775 To prepare, we introduce a pair of 2D variational quasi-functionals, $\tilde{\mathcal{A}}_{PS1}[u]$ and $\tilde{\mathcal{A}}_{PS2}[\tilde{P}]$

776 . Noting that $\tilde{P} = 0$ in the Blatter-Pattyn approximation, we drop the pressure term from

777 the transformed functional (33) and define a new pressure-free functional,

778
$$\tilde{\mathcal{A}}_{PS1}[u] = \int_V dV \left[\frac{4n}{n+1} \eta_0 \left(\tilde{\varepsilon}^2 \right)^{(1+n)/2n} + \rho g u \frac{\partial z_s}{\partial x} \right]$$
$$+ \frac{1}{2} \int_{S_{B2}} dS \, \beta(x) \left(u^2 + \zeta \left(u n_x / n_z \right)^2 \right), \tag{61}$$

779 where

780
$$\tilde{\varepsilon}^2 = \left(\frac{\partial u}{\partial x} \right)^2 + \frac{1}{4} \left(\frac{\partial u}{\partial z} + \frac{\partial w}{\partial x} \right)^2. \tag{62}$$

781 Since the continuity equation has been eliminated from (61), incompressibility is

782 introduced separately by defining a second functional,

783
$$\tilde{\mathcal{A}}_{PS2}[p] = \int_V dV \, p \left(\frac{\partial u}{\partial x} + \frac{\partial w}{\partial z} \right). \tag{63}$$

784 Note that functional (61) is a function of u, w but variation is to be taken only with

785 respect to u, and similarly, functional (63) is a function of u, w, p but variation is taken

786 only with respect to p. Direct substitution is used for boundary conditions, as before.

787 Here we are effectively viewing the pressure p as a "test function" in the finite element

788 sense. This gives us great flexibility to create elements that satisfy the solvability

789 condition (57) as desired. In a triangulation, for example, pressures may be assigned to

790 every two triangles, as in a P1-E0 grid, while others may be assigned to a single triangle

791 so as to achieve an equal number of pressure and vertical velocity variables.

792

793   The variation of $\tilde{\mathcal{A}}_{PS1}[u]$ with respect to u, results in a set of n_u discrete Euler-

794 Lagrange equations,

795
$$\hat{R}_U(u, w) = \frac{\partial \tilde{\mathcal{A}}_{PS1}(u, w)}{\partial u} = M_U(u, w) + F_U = 0. \tag{64}$$

796 This may be recognized as the Blatter-Pattyn model, (50), when w is set to zero. The

797 discrete variation of $\tilde{\mathcal{A}}_{PS2}[p]$ with respect to p, results in the continuity equation, (56),

798
$$\hat{R}_P(u,w) = \frac{\partial \tilde{\mathcal{A}}_{PS2}(u,w,p)}{\partial p} = M_{UP}^T u + M_{WP}^T w = 0 . \tag{65}$$

799 These two systems are now combined to form the BP+ approximation, as follows

800
$$\hat{R}(u,w) = \left[\hat{R}_U(u,w), \hat{R}_P(u,w) \right]^T = 0 . \tag{66}$$

801 This is a single system of $n_u + n_p$ equations to determine the $n_u + n_w$ discrete variables

802 u, w, implying that (66) is viable only on grids satisfying the solvability condition,

803 $n_p = n_w$. Just as in the standard Blatter-Pattyn approximation in §3.4.1, the vertical

804 momentum equation is missing, but instead of neglecting w, the vertical velocity is now

805 consistently obtained from the continuity equation.

806

807   The continuum version of the discrete Euler-Lagrange system (64), (65) is given

808 by

809
$$\frac{\partial}{\partial x}\left(4\tilde{\mu}\frac{\partial u}{\partial x} \right) + \frac{\partial}{\partial z}\left(\tilde{\mu}\left(\frac{\partial u}{\partial z} + \frac{\partial w}{\partial x} \right) \right) - \rho g \frac{\partial z_s}{\partial x} = 0,$$
$$\frac{\partial u}{\partial x} + \frac{\partial w}{\partial z} = 0, \tag{67}$$

810 with the boundary conditions

811
$$4\tilde{\mu}\frac{\partial u}{\partial x}n_x + \tilde{\mu}\left(\frac{\partial u}{\partial z} + \frac{\partial w}{\partial x} \right)n_z = 0 \quad \text{on } S_S, \quad u = w = 0 \quad \text{on } S_{B1},$$
$$\left. \begin{array}{l} 4\tilde{\mu}\dfrac{\partial u}{\partial x}n_x + \tilde{\mu}\left(\dfrac{\partial u}{\partial z} + \dfrac{\partial w}{\partial x} \right)n_z + \beta(x)\left(u + \zeta u\left(n_x/n_z\right)^2 \right) = 0, \\[3mm] w = -u\,n_x/n_z, \end{array} \right\} \quad \text{on } S_{B2}, \tag{68}$$

812 where $\tilde{\mu} = \eta_0\left(\tilde{\varepsilon}^2\right)^{(1-n)/2n}$ and the second invariant $\tilde{\varepsilon}^2$ is given by (62). Remarkably, this

813 same model, i.e., the BP+ approximation, was introduced by Herterich (1987) to study

814 the transition zone between an ice sheet and an ice shelf[1]. Thus, this more accurate

815 model predates the widely used Blatter-Pattyn model by some eight years but

816 unfortunately it has not received the same recognition.

817

---

[1] Reference pointed out to me by C. Schoof.

October 15, 2024

818   There are two ways of solving the BP+ system (66), as follows

819 (1) BP+, Quasi-variational, Newton iteration version:

820   Although a single variational principle does not exist in this case, it is still

821 possible to make use of Newton-Raphson iteration to obtain second order convergence.

822 To do this, we treat (66) as a single multidimensional nonlinear system and solve it using

823 Newton-Raphson iteration, as follows

824
$$
\begin{bmatrix} M_{UU}\left(u^K,w^K\right) & M_{UW}\left(u^K,w^K\right) \\ M_{UP}^T & M_{WP}^T \end{bmatrix} \begin{bmatrix} \Delta u \\ \Delta w \end{bmatrix} + \begin{bmatrix} \hat{R}_U\left(u^K,w^K\right) \\ \hat{R}_P\left(u^K,w^K\right) \end{bmatrix} = 0 , \tag{69}
$$

825 where $M_{UU}(u,w)=\partial \hat{R}_U(u,w)/\partial u$ and $M_{UW}(u,w)=\partial \hat{R}_U(u,w)/\partial w$ are the same

826 matrices as appear in (49). Convergence is rapid (quadratic) once in the basin of

827 attraction but each step is more expensive than the Picard iteration described next.

828

829 (2) BP+, Newton/Picard iteration version:

830   A single step of the Newton-Raphson system (69) may be written as follows

831
$$
\begin{aligned} M_{UU}\left(u^K,w^K\right)\Delta u + M_{UW}\left(u^K,w^K\right)\Delta w + \hat{R}_U\left(u^K,w^K\right) &= 0, \\ M_{UP}^T u^{K+1} + M_{WP}^T w^{K+1} &= 0. \end{aligned} \tag{70}
$$

832 If we lag the vertical velocity, i.e., $w^{K+1} = w^K \Rightarrow \Delta w = 0$ in the first equation, we obtain a

833 Picard iteration algorithm as follows

Starting from $K = 0,$ choose an initial guess, $u^0 \neq 0, w(u^0),$

   Solve:

834
$$
\begin{aligned} & M_{UU}\left(u^K,w^K\right)\Delta u + \hat{R}_U\left(u^K,w^K\right) = 0, \\ & u^{K+1} = u^K + \Delta u, \\ & w^{K+1} = w\left(u^{K+1}\right) = -M_{WP}^{-T} M_{UP}^T u^{K+1}, \\ & K = K+1, \end{aligned} \tag{71}
$$

   Repeat until convergence.

835 Each step of this iteration is inexpensive since it is equivalent to a step of the standard

836 Blatter-Pattyn model, (36). On the other hand, Picard iterations typically converge only

837 linearly. It remains to be seen which version is preferable in practice.

838

839   Both BP+ versions converge to the same solution. Fig. 9 compares the upper

840 surface u-velocity from the improved Blatter-Pattyn (BP+) approximation to the standard

841 Blatter-Pattyn approximation and to a reference exact Stokes calculation. The RMS u-

October 15, 2024

842   Error of the BP+ approximation relative to the exact Stokes case is shown in Fig. 12. The
843   BP+ approximation is noticeably more accurate than the BP approximation, particularly
844   in the $L = 5$ km case where the Blatter-Pattyn solution bears no resemblance to the
845   correct solution while the BP+ approximation shows excellent accuracy. This is
846   confirmed by the RMS u-Error results in Fig. 12 where BP+ is two to three times as
847   accurate as BP.
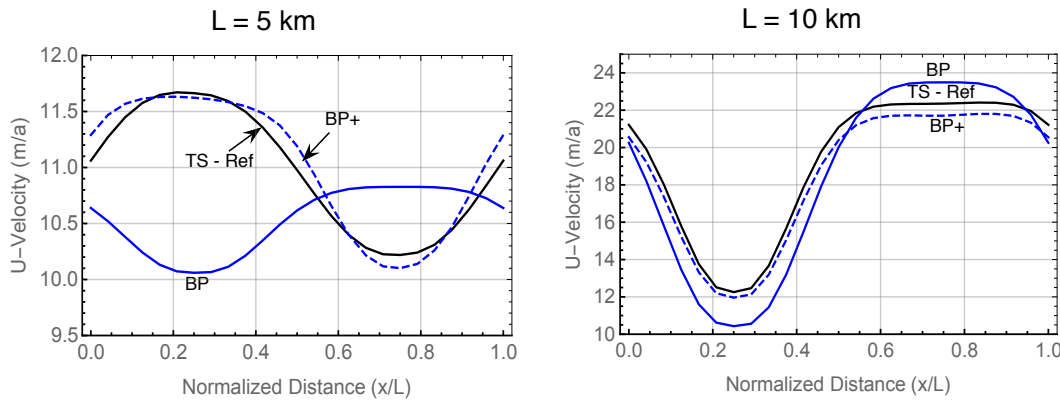
849   **Figure 9.** Comparing Approximations. Test B, Upper surface u-velocity.
850   TS-Ref: Transformed Stokes; BP: Blatter-Pattyn; BP+: Improved Blatter-Pattyn.
851   Resolution: 24x24.

853   These two versions depend on an invertible continuity equation to obtain

854    $w = w(u)$. However, vertical velocity w may already be available for the purpose of

855   temperature advection in production code packages that either incorporate or are based on
856   the Blatter-Pattyn approximation. Thus, the BP+ approximation, and particularly the
857   Newton/Picard version, may be attractive for use in such codes since they improve the
858   accuracy of the basic Blatter-Pattyn model, as seen in Fig. 9, at little additional cost.

860   **6.2.2 A "Dual-Grid" Transformed Stokes Approximation**

862   Here we take a different approach and approximate the continuity equation in the
863   transformed Stokes model, which indirectly approximates w. Thus, the continuity
864   equation is discretized on a grid coarser than the one used for the momentum equations,
865   and then interpolate the vertical velocity to appropriate locations on the finer grid. This
866   reduces the number of unknown variables in the problem, making it cheaper to solve but
867   hopefully without much loss of accuracy. As described in Appendix A, our test problem
868   grids are logically rectangular, divided into n cells horizontally and m cells vertically.
869   The coarse grid is constructed by dividing the fine grid into s equal segments in each

870 direction. This assumes that the integers n and m are each divisible by s, such that

871 there are nm/s^2 coarse cells in total, with each coarse cell containing s^2 fine cells. The

872 primary grid (i.e., the fine grid) was chosen to have $n = m = 24$, resulting in a reference

873 24×24 fine grid, so as to maximize the number of different coarse grids that may be

874 used for this test. Coarse grids were constructed using $s = 2, 3, 4, 6$, and this resulted in

875 fine/coarse grid combinations labeled by 24×12, 24×8, 24×6, 24×4, respectively.

876 Similar to a P1-E0 fine grid, coarse grid vertical velocities w are located at vertices and

877 pressures at vertical edges. Fig. 10 illustrates the case of a single coarse and four fine

878 quadrilateral cells for a grid fragment with $n = m = 2$ and $s = 1$. For the Test B problem,

879 using direct substitution for basal boundary conditions, there will be nm u-variables and

880 nm/s^2 w- and p-variables each, for a total of $nm\left(1 + 2/s^2\right)$ unknown variables,

881 considerably fewer than the $3nm$ variables in the full resolution (i.e., fine grid) case,

882 depending on the value of s. The coarse grid terms in the functional that are affected,

883 $\tilde{P}\left(\partial u/\partial x + \partial w/\partial z\right)$ and $\partial w/\partial x$, are computed using coarse grid variables and

884 interpolated to the fine grid. We will consider two versions depending on how the coarse

885 grid terms are calculated and distributed on the fine grid.

886
887

888 **Figure 10.** A Sample of a Coarse/Fine P1-E0 Grid for the Dual-Grid Approximation.

889 Resolution: $n = m = 2, s = 1$. Coarse grid is in red, fine grid in black.

890

891 (1) Approximation A, Bilinear interpolation:

892 Referring to Fig. 10, the four velocities at the vertices of the coarse grid

893 quadrilateral, i.e., u_1, u_3, u_7, u_9 and w_1, w_2, w_3, w_4, are used to obtain u, w at the remaining

894 five vertices of the fine grid by means of bilinear interpolation. Thus, the five velocities

895 u_2, u_4, u_5, u_6, u_8 are obtained in terms of vertex velocities u_1, u_3, u_7, u_9, and similarly for the

October 15, 2024

896   *w* velocities. The resulting complete set of fine grid variables, interpolated from coarse

897   grid variables, are used calculate the divergence $D = \left(\partial u / \partial x + \partial w / \partial z \right)$ and the quantity

898     $\partial w / \partial x$ in each of the eight triangular elements $t_1, t_2, \cdots, t_8$ of the fine grid. Coarse grid

899   pressures $\tilde{P}_1, \tilde{P}_2$ are associated with the coarse grid triangles T_1, T_2. The products $\tilde{P}_1 D$ in

900   elements t_1, t_2, t_3, t_5 and $\tilde{P}_2 D$ in elements t_4, t_6, t_7, t_8 are then accumulated over the entire

901   grid to obtain $\tilde{P} \left(\partial u / \partial x + \partial w / \partial z \right)$ for use in the transformed functional $\tilde{\mathcal{A}}$. Similarly, the

902   quantity $\partial w / \partial x$ is computed in the fine grid elements from coarse grid variables for use

903   in the second invariant $\tilde{\dot{\varepsilon}}^2$.

904

905   (2) Approximation B, Linear interpolation:

906   In this version, the three velocities at the vertices of the two coarse grid triangles

907   T_1 and T_2, i.e., u_1, u_3, u_7 and w_1, w_2, w_3 in T_1, and u_7, u_3, u_9 and w_3, w_2, w_4 in T_2,

908   approximate the divergence $D = \left(\partial u / \partial x + \partial w / \partial z \right)$ and the quantity $\partial w / \partial x$ as constant

909   values in the two coarse triangles. The constant quantities $\tilde{P}_1 D$, $\tilde{P}_2 D$ are then

910   accumulated over the entire grid. The constant quantity $\partial w / \partial x$ in each coarse triangle is

911   then distributed to each of the eight fine grid elements $t_1, t_2, \cdots, t_8$ depending on whether

912   the centroid of the fine triangular element is in T_1 or T_2. As in the previous case, this is

913   then used in the second invariant $\tilde{\dot{\varepsilon}}^2$ when evaluating the transformed functional $\tilde{\mathcal{A}}$.

914

915   While the number and type of unknown variables is the same in the two versions,

916   they differ considerably in accuracy, as is seen in Figs. 11 and 12. Fig. 11 compares the

917   upper surface u-velocity in both version, Approximations A and B, for the four coarse

918   grid combinations and the reference 24x24 fine grid calculation. Fig. 12 compares the

919   overall accuracy for all approximations and the transformed (TS) and standard (SS)

920   Stokes models by means of the RMS u-Error relative to the TS calculation. As might be

921   expected, the accuracy of Approx. A is better than Approx. B, particularly in the case

922   when $L = 10$ km. Both versions are more accurate than the BP and BP+ approximations,

923   except at the lowest 24x4 resolution when only Approx. A retains this distinction. Not

924   surprisingly, BP+ is more accurate than BP, but it is surprising that SS is the least

925   accurate. This is because SS is not yet converged at this resolution in Test B (see Fig. 5).

October 15, 2024
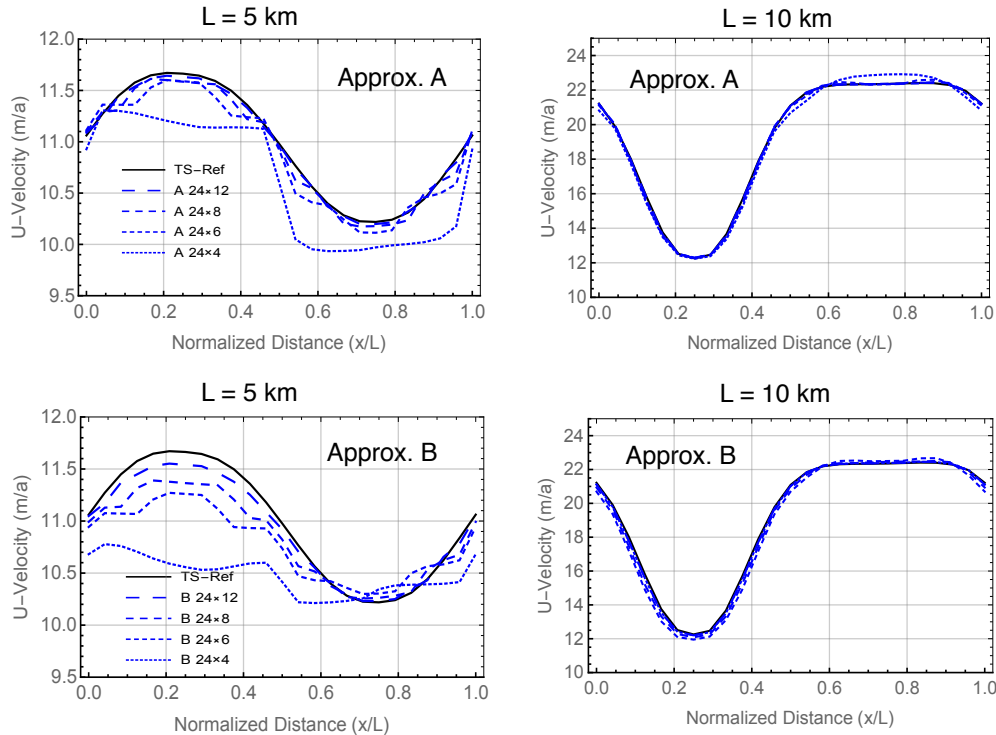
Figure 11. Comparing Approximations A and B. Test B. Upper surface u-velocity.

TS-Ref: Reference Stokes (rxr = 24x24); Fine/Coarse resolutions (rxR = 24x12, 8, 6, 4).
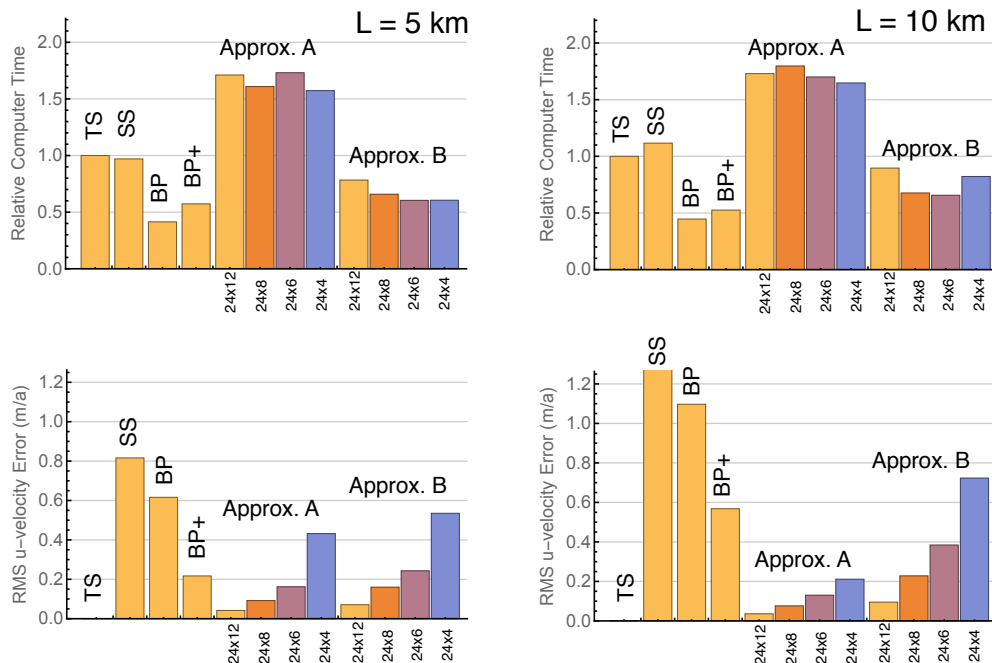
Figure 12. Comparing the Test B computer time and RMS u-Error results relative

to a TS calculation for Approximations BP, BP+, A, B, and the SS Stokes model.

TS, SS, BP, BP+: Resolution (rxr = 24x24); Approx. A, B: (rxR = 24x12, 8, 6, 4).

October 15, 2024

934

935   The computational time of the various calculations at the 24x24 resolution,

936 relative to the TS calculation, is presented in Fig. 12. This has been done reluctantly

937 because present calculations are not at all representative of the computer hardware or the

938 methods used in practical ice sheet modeling. The calculations are made on a personal

939 computer using the program Mathematica, a slow interpreted language. Thus, the

940 calculations are proof of concept only and cost comparisons are likely inaccurate and

941 possibly misleading. No effort was made to optimize the calculations or to take

942 advantage of parallelization. For example, the cost of Approximations A and B is

943 dominated by the cost of the associated interpolations, making them more costly than

944 even the unapproximated cases. However, the interpolations are highly parallelizable and

945 in practice would contribute little to the cost.

946

947 **7. Second-Order Discretizations**

948

949 So far we have been using first-order elements, primarily P1-E0. However, in current

950 practice Stokes models are more often based on second-order elements such as the

951 popular Taylor-Hood P2-P1 element (Leng et al., 2012; Gagliardini et al., 2013). In 2D

952 the P2-P1 element, illustrated in Fig. 13A, has velocities on element vertices and edge

953 midpoints and pressures on element vertices, resulting in a quadratic velocity and linear

954 pressure distributions. The element satisfies the conventional inf-sup stability condition

955 (e.g., Elman et al., 2014) but not the solvability condition (57). For example, in Test B

956 with direct substitution for basal boundary conditions, the number of vertical velocity

957 variables is $n_w = 4nm$, much larger than the number of pressure variables, $n_p = n(m+1)$.

958

959   Stokes models work well with a Taylor-Hood grid, as illustrated in Fig. 13, where

960 both P2-P1 and P1-E0 models converge to a common Test B solution, but models that

961 require the solvability condition (57) will not work on a P2-P1 grid, as is the case with

962 the extended Blatter-Pattyn approximation.   However, a second-order element can be

963 constructed that is consistent with an invertible continuity equation. This is called the

964 P2-E1 element and it is illustrated in Fig. 13A. It is second-order for velocities and linear

965 for pressure, just like the P2-P1 element, but the pressure is edge-based, as in the P1-E0

966 element. Pressure is located midway between the velocities on the vertical cell edges,

967 including an "imaginary" vertical edge joining the velocities in the middle of the vertical

968 column. Since pressures are collinear with vertical velocities along vertical grid edges, as

October 15, 2024

969 in the P1-E0 element, the same analysis in Appendix B demonstrates that this element
970 also satisfies the solvability condition (57). As explained in Appendix B, this grid should
971 be constructed using vertical columns of quadrilaterals. A 3D analog exists as explained
972 in Appendix B.

973
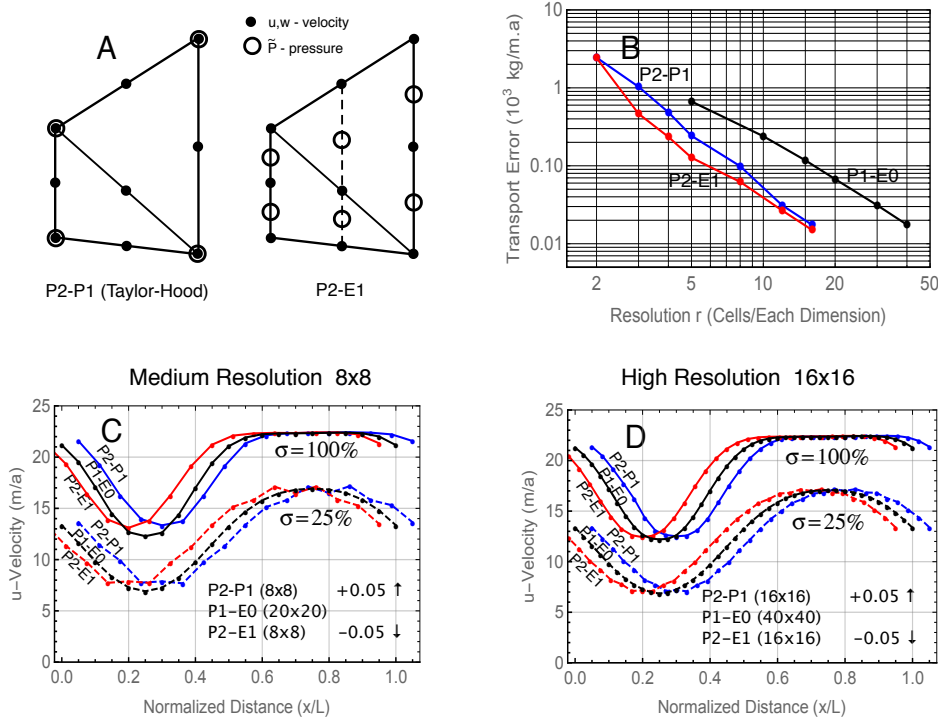
974 **Figure 13.** Comparing second-order discretizations based on the P2-P1 and P2-E1
975 elements from panel A to first-order discretizations using the P1-E0 element running Test
976 B with L=10 km. Only transformed Stokes calculations are compared; standard Stokes
977 results behave similarly. Panel B compares the convergence and accuracy of the various
978 schemes with increasing resolution, while panels C, D compare the horizontal velocities
979 at medium and maximum resolutions.

980

981 Fig. 13B shows the approximate error of the ice transport as a function of grid
982 refinement for the second-order P2-P1 and P2-E1 grids in transformed Stokes Test B
983 calculations, together with similar results for the first-order P1-E0 grid from Fig. 3, for
984 comparison. We note that both second order models show approximately the same error
985 at resolution $r = 16$ as the first order P1-E0 model at resolution $r = 40$, and similarly for
986 coarser resolutions such as $r = 8$ and $r = 20$, respectively. However, it is safe to say that
987 these second-order calculations are considerably more expensive than the first-order
988 calculations at comparable resolution or accuracy.

989

990   Panels C, D in Fig. 13 compare the u-velocities from several Test B calculations

991   using the two second-order models in comparison with first-order P1-E0 model results

992   from Fig. 3. Each panel shows results from the upper surface ($\sigma = 100\%$) in solid lines

993   and results from a surface a quarter of the way up from the bottom ($\sigma = 25\%$) in dashed

994   lines. Panel C shows results from medium resolution calculations ($r = 8, 20$ in the

995   second-order and first-order calculations, respectively) and panel D shows the

996   corresponding results from the higher resolution calculations ($r = 16, 40$). At these

997   resolutions the accuracy of the first- and second-order calculations is very similar so for

998   clarity the second-order results are displaced horizontally from the first-order results by

999   0.05 nondimensional units. The P2-E1 results in magenta are displaced to the left and the

1000   P2-P1 results in blue are displaced to the right. In general, models satisfying the

1001   solvability condition, namely the P1-E0 and P2-E1 models, are better behaved than the

1002   P2-P1 model. This is possibly related to the well-known "weak" mass conservation of

1003   the Taylor-Hood element. This problem is greatly improved by "enriching" the pressure

1004   space with constant pressures in each triangular element (Boffi et al., 2012). In the 2D

1005   Test B problem this increases the number of pressure variables from $n_p = n(m+1)$ in the

1006   basic Taylor-Hood element to $n(3m+1)$, much closer to the $4nm$ needed to satisfy the

1007   solvability condition. On the other hand, the pressure in the P2-E1 case is highly

1008   oscillatory but well behaved in the P2-P1 case. However, this is not at all concerning

1009   since the transformed pressure, a Lagrange multiplier, has no physical significance.

1010

1011   **8. A Summary and Discussion**

1012

1013   In summary, this paper presents two innovations in ice sheet modeling. The first

1014   innovation involves a transformation of the ice sheet Stokes equations into a form that

1015   differs from the approximate Blatter-Pattyn system by a small number of terms. In

1016   particular, the variational formulations differ from the Blatter-Pattyn case only by the

1017   absence of the vertical velocity w in the second invariant of the strain rate tensor.

1018

1019   We focus on two applications of the new transformation. First, these extra terms

1020   in the transformed Stokes equations may be "switched" on or off to convert the code

1021   from a full-Stokes model to a Blatter-Pattyn model, if desired. Additionally, ice sheet

1022   flows are generally shallow but often contain limited areas where Stokes equations must

1023   be solved. Thus, the switch from Blatter-Pattyn to Stokes may be done locally and

1024   adaptively only where the extra accuracy is required. Second, the fact that neglecting the
1025   vertical velocity in only one localized place creates the Blatter-Pattyn approximation
1026   suggests that if instead the vertical velocity is approximated will result in improved
1027   approximations. We present two such approximations. The first approximation, called
1028   the BP+ approximation, solves the pressure-free horizontal momentum equation with the
1029   vertical velocity obtained from the continuity equation. Remarkably, the BP+
1030   approximation is actually the same as a model originally proposed by Herterich (1987).
1031   The second approximation approximates the vertical velocity simply by discretizing the
1032   continuity equation on a coarser grid than the rest of the model.

1033

1034   The second innovation involves the introduction and use of finite element
1035   discretizations that feature a decoupled invertible continuity equation permitting the
1036   numerical solution for the vertical velocity in terms of the horizontal velocity
1037   components, i.e., $w = w(u,v)$. Some examples of such grids for use in 2D and 3D are
1038   given in Appendix B. An important example is the P1-E0 grid that is used in most of the
1039   test problems in this paper. However, one can alternatively obtain $w = w(u,v)$ by other
1040   means, as for example by discretizing (43). For example, this is done in MALI (Hoffman
1041   et al., 2018), a code based on the Blatter-Pattyn approximation, to obtain the vertical
1042   velocity w for the advection of ice temperature (Mauro Perego, private communication).

1043

1044   **Code Availability**

1045

1046   All calculations were made using the Wolfram Research, Inc. program Mathematica in a
1047   development environment. A large number of Mathematica Notebooks were used to
1048   produce the different results. A representative Notebook (a ‚nb file) is available in a
1049   public repository at https://doi.org/10.5281/zenodo.13940989 for a Test D^* calculation
1050   (described in Appendix A) at $L = 10\,\text{km}$ and a resolution of 20x20. This test problem
1051   was chosen to demonstrate the use of direct substitution for the tangency basal boundary
1052   condition, (14), in the functional. A Mathematica Notebook may be viewed by
1053   downloading the free Wolfram Player from https://www.wolfram.com/player/ but the full
1054   Mathematica code is required for editing or execution.

1055

1056 **Competing Interests**

1057

1058 The author has acknowledged that there are no competing interests.

1059

1060 **Acknowledgements**

1061

1062 I am grateful to Steve Price for support, and especially to Mauro Perego, William (Bill)

1063 Lipscomb, and reviewers Ed Bueler and Christian Schoof for many helpful comments

1064 and suggestions that helped to improve the paper.

1065

1066 **References**

1067

1068 Auricchio, F., da Veiga, L.B., Brezzi, F., and Lovadina, C.: Mixed Finite Element

1069 Methods, In Encyclopedia of Computational Mechanics Second Edition (Eds E. Stein, R.

1070 de Borst, and T.J.R. Hughes), John Wiley & Sons, Ltd., 2017.

1071

1072 Blatter, H.: Velocity and Stress Fields in Grounded Glaciers: A Simple Algorithm for

1073 Including Deviatoric Stress Gradients, J. Glaciol., 41, 333-344, 1995.

1074

1075 Boffi, D., Brezzi, F., Fortin, M.: Finite Elements for the Stokes Problem. In: Boffi D.,

1076 Gastaldi L. (eds) Mixed Finite Elements, Compatibility Conditions, and Applications.

1077 Lecture Notes in Mathematics, vol 1939. Springer, Berlin, Heidelberg.

1078 https://doi.org/10.1007/978-3-540-78319-0_2, 2008.

1079

1080 Boffi, D., Cavallini, N., Gardini, F., and Gastaldi, L.: Local Mass Conservation of Stokes

1081 Finite Elements, J. Sci. Comput., 52, 383–400, 2012.

1082

1083 Chen, Q., Gunzburger, M., and Perego, M.: Well-Posedness Results for a Nonlinear

1084 Stokes Problem Arising in Glaciology, SIAM J. Math. Anal., 45(5), 2710-2733, 2013.

1085

1086 Cheng, G., Lötstedt, P., and von Sydow, L.: A Full Stokes Subgrid Scheme in Two

1087 Dimensions for Simulation of Grounding Line Migration in Ice Sheets Using Elmer/ICE

1088 (v8.3), Geosci. Model Dev., 13, 2245-2258, 2020.

1089

1090 Dukowicz, J.K., Price, S.F., and Lipscomb, W.H.: Consistent Approximations and
1091 Boundary Condition for Ice Sheet Dynamics from a Principle of Least Action, J. Glaciol.,
1092 56, 480-496, 2010.

1094 Dukowicz, J.K., Price, S.F., and Lipscomb, W.H.: Incorporating Arbitrary Basal
1095 Topography in the Variational Formulation of Ice Sheet Models, J. Glaciol., 57, 461-467,
1096 2011.

1098 Dukowicz, J.K.: Refolmulating the Full-Stokes Ice Sheet Model for a More Efficient
1099 Computational Solution, The Cryosphere, 6, 21-34, 2012.

1101 Elman, H.C., D.J. Silvester, and A.J. Wathen, 2014: *Finite Elements and Fast Iterative*
1102 *Solvers: With Applications in Incompressible Fluid Dynamics*, 2nd Ed., Oxford
1103 University Press, 494 pp.

1105 Gagliardini, O., and Zwinger, T.: The ISMIP-HOM Benchmark Experiments Performed
1106 Using the Finite-Element Code Elmer, The Cryosphere, 2, 67–76, 2008.

1108 Gagliardini, O., Zwinger, T., Gillet-Chaulet. F., Durand, G., Favier, L., de Fleurian, B.,
1109 Greve, R., Malinen, M., Martín, C., Råback, P., Ruokolainen, J., Sacchettini, M., Schäfer,
1110 M., Seddik, H., and Thies, J.: Capabilities and Performance of Elmer/Ice, a New-
1111 Generation Ice Sheet Model, Geosci. Model Dev., 6, 1299–1318, doi:10.5194/gmd-6-
1112 1299-2013, 2013.

1114 Greve, R. and Blatter, H.: Dynamics of Ice Sheets and Glaciers, Springer-Verlag, Berlin
1115 Heidelberg, 2009.

1117 Heinlein, A., Perego, M., and Rajamanickam, S.: FROSch Preconditioners for Land Ice
1118 Simulations of Greenland and Antarctica, SIAM J. Sci. Comput., 44, V339-B367, doi:
1119 10.1137/21M1395260, 2022.

1121 Herterich, K.: On the Flow Within the Transition Zone Between Ice Sheet and Ice Shelf,
1122 in Dynamics of the West Antarctic Ice Sheet, Proceedings of a workshop held in Utrecht,
1123 May 6-8, 1985, (Eds. C. J. Van Der Veen and J. Oerlemans), D. Reidel, Dordrecht, 185-
1124 202, 1987.

October 15, 2024

1125

1126 Hoffman, M. J., Perego, M., Price, S. F., Lipscomb, W. H., Zhang, T., Jacobsen, D.,

1127 Tezaur, I., Salinger, A. G., Tuminaro, R., and Bertagna, L.: MPAS-Albany Land Ice

1128 (MALI): A Variable-Resolution Ice Sheet Model for Earth System Modeling Using

1129 Voronoi Grids, Geosci. Model Dev., 11, 3747–3780, doi:10.5194/gmd-11-3747-2018,

1130 2018.

1131

1132 Hood, P. and Taylor, C.: Numerical Solution of the Navier-Stokes Equations Using the

1133 Finite Element Technique, Comput. Fluids, 1, 1-28, 1973.

1134

1135 Larour, E., Seroussi, H., Morlighem, M., and Rignot, E.: Continental scale, high order,

1136 high spatial resolution, ice sheet modeling using the Ice Sheet System Model (ISSM), J.

1137 Geophys. Res., 117, 1–20, doi:10.1029/2011JF002140, 2012.

1138

1139 Leng, W., Ju, L., Gunzburger, M., Price, S., and Ringler, T.: A Parallel High-Order

1140 Accurate Finite Element Nonlinear Stokes Ice Sheet Model and Benchmark Experiments,

1141 J. Geophys. Res., 117, 2156–2202, doi:10.1029/2011JF001962, 2012.

1142

1143 Lipscomb, W.H., Price, S.F., Hoffman, M.J., Leguy, G.R., Bennett, A.R., Bradley, S.L.,

1144 Evans, K.J., Fyke, J.G., Kennedy, J.H., Perego, M., Ranken, D.M., Sacks, W.J., Salinger,

1145 A.G., Vargo, L.J., and Worley, P.H.: Description and Evaluation of the Community Ice

1146 Sheet Model (CISM) v. 2.1, Geosci. Model Dev., 12, 387-424, 2019.

1147

1148 Nowicki, S.M.J. and Wingham, D.J.: Conditions for a Steady Ice Sheet-Ice Shelf

1149 Junction, *Earth Planet. Sci. Lett.*, **265**(1-2), 246-255, 2008.

1150

1151 Pattyn, F.: A New Three-Dimensional Higher-Order Thermomechanical Ice Sheet

1152 Model: Basic Sensitivity, Ice Stream Development, and Ice Flow across Subglacial

1153 Lakes, J. Geophys. Res., 108(B8), 2382, 2003.

1154

1155 Pattyn, F., Perichon, L., Aschwanden. A., Breuer, B., de Smedt, B., Gagliardini, O.,

1156 Gudmundsson, G.H., Hindmarsh, R.C.A., Hubbard, A., Johnson, J.V., Kleiner, T.,

1157   Konovalov, Y., Martin, C., Payne, A.J., Pollard, D., Price, S., Ruckamp, M., Saito, F.,

1158   Soucek, O., Sugiyama, S., and Zwinger, T.: Benchmark Experiments for Higher-Order

1159   and Full-Stokes Ice Sheet Models (ISMIP–HOM), The Cryosphere, 2, 95-108, 2008.

1160

1161   Perego, M., Gunzburger. M., and Burkardt, J.: Parallel Finite-Element Implementation

1162   for Higher-Order Ice-Sheet Models, J. Glaciol., 58, 76-88, 2012.

1163

1164   Rückamp, M., Kleiner, T., and Humbert, A.: Comparison of ice dynamics using full-

1165   Stokes and Blatter-Pattyn approximation: application to the Northeast Greenland Ice

1166   Stream, The Cryosphere, 16, 1675-1696, 2022.

1167

1168   Schoof, C.: Coulomb friction and other sliding laws in a higher order glacier flow model,

1169   Math. Models. Meth. Appl. Sci., 20(1), 157–189, 2010.

1170

1171   Schoof, C. and Hewitt, I.: Ice-Sheet Dynamics, Annu. Rev. Fluid Mech., 45, 217–239,

1172   2013.

1173

1174   Schoof, C. and Hindmarsh, R.C.A.: Thin-Film Flows with Wall Slip: An Asymptotic

1175   Analysis of Higher Order Glacier Flow Models, Quart. J. Mech. Appl. Math, 63, *73-114*,

1176   2010.

1177

1178   Seroussi, H., Ben Dhia, H., Morlighem, M., Latour, E., Rignot, E., and Aubry, D.:

1179   Coupling Ice Flow Models of Varying Orders of Complexity with the Tiling Method, J.

1180   Glaciol., 58, 776-786, 2012.

1181

1182   Tezaur, I. K, Perego, M., Salinger, A. G., Tuminaro, R. S., and Price, S. F.:

1183   Albany/FELIZ: A Parallel, Scalable and Robust, Finite Element, First-Order Stokes

1184   Approximation Ice Sheet Solver Built for Advanced Analysis, Geosci. Model Dev., 8,

1185   1197-1220, 2015.

1186

1187   **Appendix A: Test Problems**

1188

1189   We will use three 2D test problems to demonstrate the new methods. The geometrical

1190   configuration of the three problem grids is illustrated in Fig. A1. The first problem, Test

1191   B, is actually Exp. B from the ISMIP-HOM benchmark suite (Pattyn et al., 2008); it

October 15, 2024

1192   features a no-slip condition (infinite friction) on a sinusoidal basal surface. The second

1193   problem, Test D*, incorporating sinusoidal friction along a uniformly sloped plane basal

1194   surface, is a replacement with modified parameters for Exp. D from the benchmark suite

1195   since ice flow in Exp. D is nearly vertically uniform (see Fig. 4), more characteristic of a

1196   shallow-shelf approximation, and this is rectified by increased basal friction.
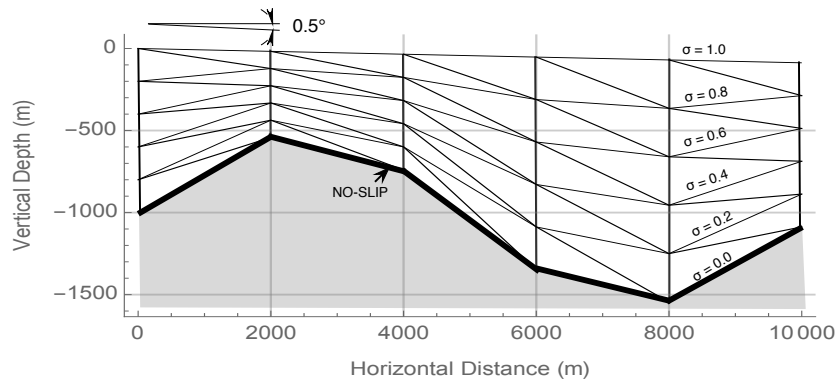
ISMIP-HOM Test Problem B - No Slip
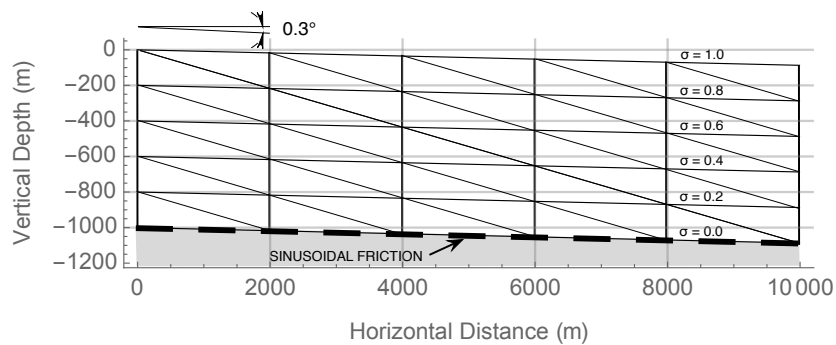
Test Problem D* - Sinusoidal Friction
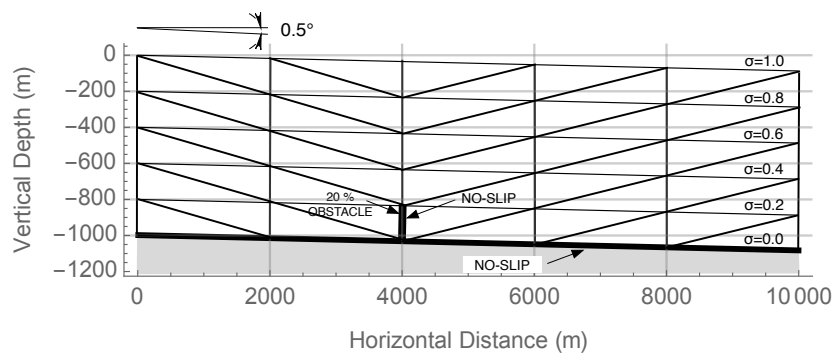
Test Problem O - 20% Obstacle - No Slip

1197

1198   **Figure A1.** Test problem grids. For clarity, a coarse 5x5 configuration is shown.

1199

1200   A third problem, Test O (for "Obstacle") is introduced to illustrate adaptive

1201   switching discussed in §6.1. Test O has a unique feature, namely, a thin no-slip obstacle,

1202 located at $x = 4\,km$ and extending vertically $200\,m$ from the bed (20 % of the ice sheet

1203 thickness), as illustrated in Fig. A1, which forces the ice flow near the obstacle to adjust

1204 abruptly. Because of the no-slip boundary conditions along the obstacle surface, a

1205 triangular element in the lee of the obstacle, with one vertical edge and one edge along

1206 the bed, would have all zero vertex velocities. This implies zero stress and therefore a

1207 local singularity in ice viscosity. To avoid this, all elements at the back of the obstacle

1208 are "reversed" as compared to the ones at the front of the obstacle, as shown in Fig. A1.

1209

1210 All tests feature a sloping flat upper surface, given by $z_s(x) = -x\,\mathrm{Tan}(\theta)$, where

1211 $\theta = 0.5°$ for Tests B and O, and $\theta = 0.3°$ for Test D* (this differs from the $0.1°$ slope in

1212 Test D), with a free-stress upper boundary condition in all cases. The sinusoidal bottom

1213 surface elevation for Test B is specified by $z_b(x) = z_s(x) - H_0 + H_1\,\mathrm{Sin}(\omega x)$, where the

1214 depth $H_0 = 1000\,m$, $H_1 = 500\,m$, $\omega = 2\pi/L$, and L is the perturbation wavelength,

1215 which is also the domain length. The bottom surface elevation in Tests D* and O is

1216 $z_b(x) = z_s(x) - H_0$, parallel to the upper surface. The length L in the ISMIP-HOM suite

1217 ranges from $5\,km$ to $160\,km$, but here we consider only the two cases at the high end of

1218 the aspect ratio H_0/L range, namely, $L = 5\,km$ and $L = 10\,km$, where the inaccuracy of

1219 the Blatter-Pattyn approximation becomes noticeable. In all cases the lateral boundary

1220 conditions are periodic. The spatially varying friction coefficient for Test D* is given by

1221 $\beta(x) = \beta_0 + \beta_1\,\mathrm{Sin}(\omega x)$, where $\beta_0 = \beta_1 = 10^4\,Pa\,a\,m^{-1}$ (these are an order of magnitude

1222 higher than in Test D). The physical parameters are the same as in ISMIP-HOM,

1223 namely, ice-flow parameter $A = 10^{-16}\,Pa^{-3}a^{-1}$, ice density $\rho = 910\,kg\,m^{-3}$, and

1224 gravitational constant $g = 9.81\,ms^2$. In general, units are MKS, except where time is

1225 given per annum, convertible to per second by the factor $3.1557 \times 10^7\,s\,a^{-1}$.

1226

1227 **Appendix B: Grids Satisfying the Solvability Condition**

1228 **B1 An Invertible Continuity Equation**

1229

1230 As discussed in §4, the invertibility of the discrete continuity equation requires special

1231 grids that satisfy the solvability condition. Here we discuss several such grids and their

1232 properties. Fig. B1 shows three 2D elements on triangles or quadrilaterals that satisfy the

October 15, 2024

1233 solvability condition (57) in certain circumstances. The P1-E0 element is quite general,

1234 as demonstrated in §B2. It has velocities located at triangle vertices, resulting in a linear

1235 velocity distribution within each triangle (P1), and pressure located on the vertical edge

1236 of each triangle, providing a constant pressure over the two triangles that share that edge

1237 (E0). A second order version of this element, the P2-E1 element, is shown in Fig. 13A.

1238 The other two elements, the P1-Q0 and Q1-Q0 elements, satisfy the solvability condition

1239 when used in Tests B and D* but may not do so in other problems. The P1-Q0 element

1240 also has velocities on triangle vertices for a linear velocity distribution within each

1241 triangle (P1) but the pressure is constant within the quadrilateral (Q0) formed by the two

1242 adjoining triangles. The Q1-Q0 element has velocities located at quadrilateral vertices

1243 and pressure centered in the quadrilateral, resulting in a bi-quadratic velocity distribution

1244 (Q1) and a constant pressure within the quadrilateral (Q0).

1245
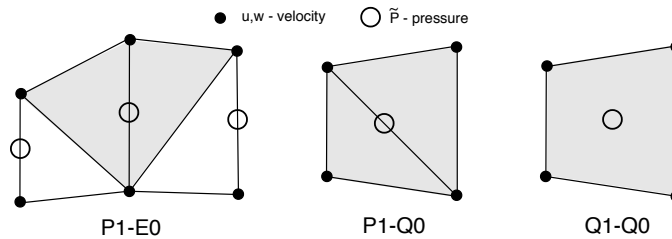
1246 **Figure B1.** Three first-order 2D elements that may be used to satisfy the

1247 solvability condition, (57), in Tests B and D*.

1248

1249 The solutions are stable, as expected, and they all converge with the same value

1250 for ice transport. The pressure distribution is smooth in the P1-E0 case, but contains

1251 small fluctuations near the upper surface in the P1-Q0 and Q1-Q0 cases that tend to

1252 disappear as resolution is increased. The Q1-Q0 element is unstable in conventional

1253 applications because it contains a checkerboard pressure null space and is only used in a

1254 stabilized form (see Elman et al., 2014, where the element is called Q1-P0). Here,

1255 however, the Q1-Q0 grid does behave well, presumably because it satisfies the solvability

1256 condition. Overall, this confirms our expectation of stability when the solvability

1257 condition is satisfied. As we discuss next, the P1-E0 element is special because the

1258 solvability condition is satisfied along each vertical edge, as opposed to being satisfied

1259 over the entire grid as in the other two elements.

1260

1261 **B2 The Solvability Condition in the P1-E0 Element**

1262 Fig. B2 illustrates the P1-E0 element used in a representative grid. We assume

1263 that the grid is composed of vertical columns subdivided into triangular elements.

October 15, 2024

1264 Consider a single vertical edge from bottom to the top. Assuming there are m edge

1265 segments in the vertical direction, there will be $m+1$ discrete w variables and m discrete

1266 $\tilde{P}$ variables since each $\tilde{P}$ variable is located between a pair of w variables. However,

1267 since the w variable at the bed is specified as a boundary condition, either directly as a

1268 no-slip condition or as part of a no-penetration condition, there will be only m unknown

1269 w variables. As a result we have $n_w = n_p$ along each vertical grid edge, and therefore

1270 over the entire grid, satisfying the solvability condition. In case Lagrange multipliers are

1271 used, there will be $m+1$ unknown discrete w variables (since now the basal vertical

1272 velocity w is also an unknown). However, this is matched by m unknown $\tilde{P}$ variables,

1273 supplemented by one λ_z or one Λ unknown Lagrange multiplier variable, depending on

1274 the type of boundary condition. Thus, again the number of unknown variables equals the

1275 number of equations along every vertical edge, thereby satisfying the solvability

1276 condition whether Lagrange multipliers are used or not. This means that the P1-E0

1277 element can be used to satisfy the solvability condition irrespective of the boundary

1278 conditions on quite arbitrary grids, as illustrated in Fig. B2. These arguments apply for

1279 other versions of the P1-E0 element as well, such as the second order version P2-E1 in

1280 Fig. 13A or the 3D version in Fig. B3.

1281
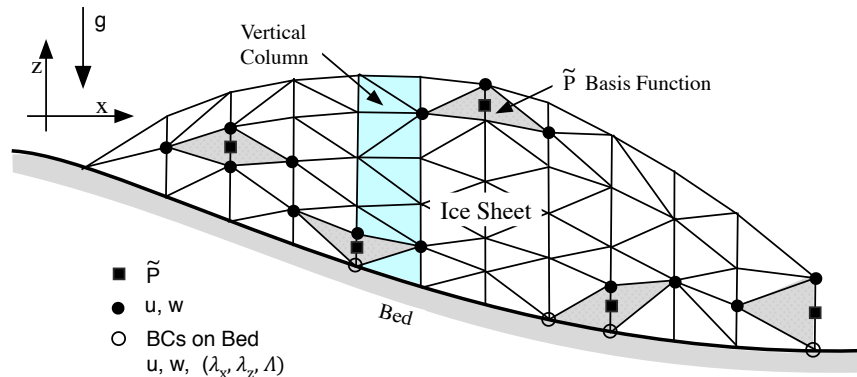
1282 **Figure B2.** An illustration of a 2D edge-based P1-E0 grid, composed of vertical columns

1283 randomly subdivided into triangles. Pressures are located on the vertical edges. The

1284 triangulation and the configuration of the pressure basis functions (shown in gray)

1285 is quite general, allowing for a flexible triangulation of the domain.

1286

1287 **B3 Two- and Three-Dimensional Meshes Based on the P1-E0 Element**

1288 The P1-E0 element has been used on the test problem grids in Fig. A1 and

1289 performs well. Moreover, the element has great geometric generality, as in Fig. B2, so it

October 15, 2024

1290   may be used for quite complicated grids. Generally, there are two triangles associated

1291   with a pressure variable, one on each side of a vertical edge, except in situations where

1292   the ice sheet ends at a vertical face, as in Fig. B2. However, there is no problem since the

1293   pressure is simply associated with the single triangle on one side of the vertical face.

1294

1295   Meshes composed of P1-E0 elements have another useful property. Since

1296   pressure and vertical velocity variables alternate along vertical grid lines, the matrix-

1297   vector products $M_{WP}p$, $M_{WP}^T w$ in (47), corresponding to $\partial\tilde{P}/\partial z$ and $\partial w/\partial z$ in the

1298   vertical momentum and continuity equations, respectively, consist of simple decoupled

1299   bi-diagonal one-dimensional difference equations along each vertical grid line for

1300   determining pressure and vertical velocity. This should be particularly advantageous for

1301   parallelization.

1302
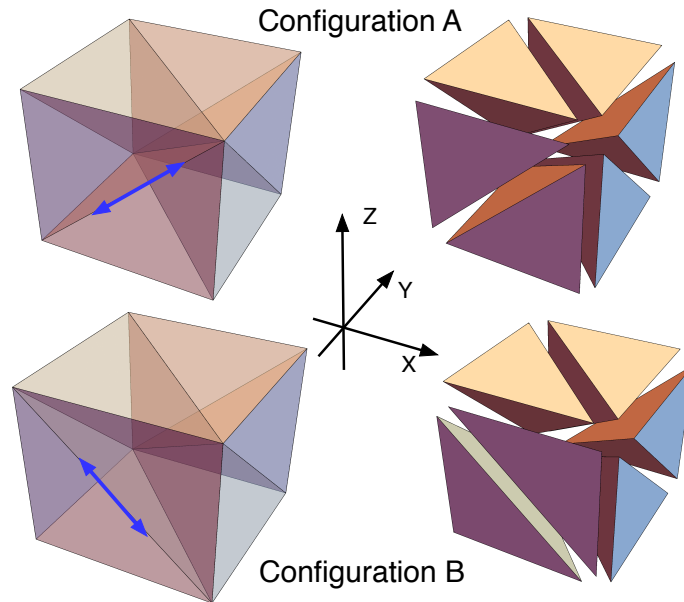
1303   **Figure B3.** Three-dimensional P1-E0 tetrahedral elements that generalize the 2D

1304   P1-E0 element of Fig. C1. Configurations A and B differ by having an internal

1305   triangular face rotated, as indicated by the blue arrows. Both configurations

1306   satisfy the solvability condition.

1307

1308   The two-dimensional P1-E0 element has a relatively simple three-dimensional

1309   counterpart, shown in Fig. B3. The mesh again consists of vertical columns, this time

1310   composed of hexahedra. Each hexahedron is subdivided into six tetrahedra such that

1311   each vertical edge is surrounded by as few as four to as many as eight tetrahedra. As in

1312   the 2D case, velocity components are collocated at vertices, yielding a piecewise-linear

October 15, 2024

1313   velocity distribution in each tetrahedral element, and pressures are located in the middle

1314   of each vertical edge so that pressure is constant in the tetrahedra that surround that edge.

1315   Lagrange multipliers, if used, are located at the vertices on the basal surface, yielding a

1316   piecewise linear distribution on the basal triangular facet. Since pressures and vertical

1317   velocities are again intermingled along a single line of vertical edges from top to bottom,

1318   we see that this satisfies the solvability condition (57) since the argument used in the 2D

1319   case applies here also.

1320

1321   Fig. B3 shows two of the several possible configurations of a typical hexahedron,

1322   including an exploded view of each configuration for clarity. The two configurations

1323   differ in having the internal face of the two forward-facing tetrahedra rotated, creating

1324   two different forward facing tetrahedra. The remaining six tetrahedra are undisturbed.

1325   Since edges must align when hexahedra (or tetrahedra) are connected, this shows that the

1326   3D mesh can be flexibly reconnected and rearranged, just as in the 2D case of Fig. B2.

1327

1328   **Remark #3**: A closely related but perhaps even simpler three-dimensional P1-E0

1329   element is one used in Leng et al. (2012) that is based on the P2-P1 prismatic tetrahedral

1330   element. A grid of these elements is composed of vertical columns of triangular prisms

1331   (with triangular faces at the top and bottom), each subdivided into three tetrahedra.

1332   Pressures are located on the vertical prism edges, as in Fig. B3, so this again satisfies the

1333   solvability condition.

1334

1335   Just as the 2D second-order P2-E1 element in Fig. 13A is a generalization of the

1336   P1-E0 element, a 3D second-order P2-E1 element may be constructed as a generalization

1337   of the P1-E0 element illustrated in Fig. B3. Velocities would be located at the vertices

1338   and at midpoints of the tetrahedral edges, and pressures halfway between the velocities

1339   on vertical edges, including the imaginary vertical edges through the midpoints of the

1340   tetrahedral edges, in the same way as in the 2D case in Fig. 13A. The P2-E1 element in

1341   both 2D and 3D would also satisfy the solvability condition since the arguments in §B2

1342   apply here as well because pressures are again located midway between vertical

1343   velocities along all vertical edges.

October 15, 2024